

1 **Illuminating the pre-, co-, and post-seismic phases of**  
2 **the 2016 M7.8 Kaikōura earthquake with 10 years of**  
3 **seismicity**

4 **C. J. Chamberlain<sup>1</sup>, W. B. Frank<sup>2</sup>, F. Lanza<sup>3</sup>, J. Townend<sup>1</sup>, E. Warren-Smith<sup>4</sup>**

5 <sup>1</sup>School of Geography, Environment and Earth Sciences, Victoria University of Wellington, Wellington,  
6 New Zealand

7 <sup>2</sup>Department of Earth, Atmospheric and Planetary Sciences, Massachusetts Institute of Technology,  
8 Cambridge, MA, USA

9 <sup>3</sup>Swiss Seismological Service, ETH Zürich, Switzerland

10 <sup>4</sup>GNS Science, Lower Hutt, New Zealand

11 **Key Points:**

- 12 • 10 year-long matched-filter derived-catalog of 33,328 earthquakes surrounding the  
13 2016 Kaikōura earthquake.  
14 • Observed offshore reverse faulting provides a direct and viable rupture pathway.  
15 • No detectable seismicity occurs on the subduction interface, and any deformation  
16 there is aseismic.

---

Corresponding author: Calum J. Chamberlain, [calum.chamberlain@vuw.ac.nz](mailto:calum.chamberlain@vuw.ac.nz)

**Abstract**

The 2016 M7.8 Kaikōura earthquake is one of the most complex earthquakes in recorded history, with significant rupture of at least 21 crustal faults. Using a matched-filter detection routine, precise cross-correlation pick corrections, and accurate location and re-location techniques, we construct a catalog of 33,328 earthquakes between 2009 and 2020 on and adjacent to the faults that ruptured in the Kaikōura earthquake. We also compute focal mechanisms for 1,755 of the earthquakes used as templates. Using this catalog we reassess the rupture pathway of the Kaikōura earthquake. In particular we show that: (1) the earthquake nucleated on the Humps Fault; (2) there is a likely linking offshore reverse fault between the southern fault system and the Papatea Fault, which could explain the anomalously high slip on the Papatea Fault; (3) the faults that ruptured in the 2013 Cook Strait sequence were reactivated by the Kaikōura earthquake and may have played a role in the termination of the earthquake; and (4) no seismicity on an underlying subduction interface is observed beneath almost all of the ruptured region suggesting that if deformation did occur on the plate interface then it occurred aseismically and did not play a significant role in generating co-seismic ground motion.

**Plain Language Summary**

The 2016 Kaikōura earthquake in the South Island of New Zealand, is one of the most complex earthquakes reported. While extensive geological work has been undertaken to map the surface faulting in the earthquake, it remains unclear how these faults are linked together at depth. In this paper we document the construction of a dense, long-duration catalog of earthquakes that occurred on and around the faults that slipped in the Kaikōura earthquake. Using this catalog of 33,328 earthquakes we are able to illuminate likely sub-surface links between faults and investigate how these faults slipped before and after the Kaikōura earthquake. We show that offshore faults provide a link between the southern faults, where the earthquake started, and the northern faults, where the highest slip occurred. We also show that the earthquake stopped on faults that had previously slipped in the 2013 Cook Strait earthquakes, and which likely played a role in earthquake arrest. Finally we see no evidence for elevated seismicity on the underlying subduction interface beneath the faults that slipped in the Kaikōura earthquake.

**1 Introduction**

The November 2016 Kaikōura M 7.8 earthquake ruptured at least 21 faults in the Marlborough Fault Zone at the transition from subduction on the Hikurangi subduction zone to on-land transpression (Figure 1; Kaiser et al., 2017; Hamling et al., 2017; Litchfield et al., 2018). This complex earthquake involved a wide range of co-seismic faulting styles, producing dextral, sinistral, reverse and normal surface ruptures (Clark et al., 2017). In addition to the extensive crustal faulting, the underlying subduction interface may have slipped co-seismically (Bai et al., 2017; T. Wang et al., 2018), although regional data show little evidence for this (Hamling et al., 2017; Holden et al., 2017).

The transpressional rupture cascade resulted in significant surface rupture of multiple previously known and unknown faults (Litchfield et al., 2018). The complexity of the earthquake rupture (Hamling et al., 2017) has to date precluded the robust constraint of the role of individual faults within the rupture sequence (e.g. Holden et al., 2017) and the dynamics of the rupture propagation and termination (Ando & Kaneko, 2018; Ulrich et al., 2019). When modelling such complex ruptures, the identification of all major participating faults has a significant impact on where the inferred slip is concentrated (e.g. Hamling et al., 2017) and the propagation sequence from one fault to the next, exemplified by the different rupture pathways modelled by Ando and Kaneko (2018) and Ulrich et al. (2019). The implications of these models are wide ranging: from a general

66 understanding of how earthquakes are able to propagate through complex fault systems,  
67 to more local implications for seismic hazard in central New Zealand.

68 Almost all published models of co-seismic and post-seismic deformation in the Kaikōura  
69 earthquake have been based on simplified fault models derived from near-surface geo-  
70 logical data (e.g. Hamling et al., 2017; Xu et al., 2018; T. Wang et al., 2018; Holden et  
71 al., 2017; Clark et al., 2017). While these data provide essential controls, they do not  
72 provide robust information on the fault structure at depth, where most of the slip hap-  
73 pens during earthquakes. Accurate earthquake catalogs provide a viable tool to constrain  
74 fault geometry at depth (e.g. Plesch et al., 2020), but have thus far been unavailable for  
75 the Kaikōura region, apart from the relatively small catalog developed by Lanza et al.  
76 (2019), and sparse moment tensor analysis by Cesca et al. (2017). Such catalogs of seis-  
77 micity can also help illuminate other elements of the Kaikōura earthquake, including its  
78 relationship to prior seismicity in New Zealand, and how the various faults respond post-  
79 seismically.

### 80 1.1 Co-seismic kinematics and rupture propagation

81 Kinematic rupture models (Holden et al., 2017) show that the Kaikōura rupture  
82 started slowly on the Humps–Hundalee Fault system (Nicol et al., 2018; J. N. Williams  
83 et al., 2018). However, hypocentre estimates of the Kaikōura earthquake vary from be-  
84 ing consistent with nucleation on the Humps Fault (Lanza et al., 2019; Nicol et al., 2018),  
85 to being as much as 7–15 km off the Humps Fault (according to the GeoNet<sup>1</sup> and USGS  
86 solutions respectively<sup>2</sup>).

87 Once initiated, the rupture propagated north-east towards the Hope Fault, but only  
88 produced a minor surface rupture (Hamling et al., 2017; Litchfield et al., 2018) of this  
89 fault, which previous paleoseismic studies have indicated to have a high Quaternary slip-  
90 rate (Litchfield et al., 2018). The rupture then stepped onto the Jordan Thrust–Kekerengu  
91 system where the maximum co-seismic surface offset of 11.8 m dextral occurred on the  
92 Kekerengu Fault (Kearse et al., 2018). The dominantly N–S-striking Papatea Fault, which  
93 intersects the junction between the Jordan Thrust and the Kekerengu Fault, also rup-  
94 tured with up to 9.5 m of uplift and 6.1 m of sinistral motion (R. M. Langridge et al.,  
95 2018). Previous authors (e.g. Hamling et al., 2017; Holden et al., 2017) have noted that  
96 the high slip on the short (c. 19 km long) Papatea fault cannot be fit by elastic rupture  
97 models. The Papatea Fault intersects the Jordan Thrust–Kekerengu system at the point  
98 where dextral slip increases from the Jordan Thrust to the Kekerengu, and on-fault dip-  
99 slip motion changes sense, from normal on the Jordan Thrust to reverse on the Kekerengu  
100 (Kearse et al., 2018). This normal motion (NW down) on the Jordan Thrust appears  
101 not to be the dominant long-term sense of motion, with higher mountains on the NW  
102 side attesting to the dominantly oblique-reverse motion on the Jordan Thrust and Up-  
103 per Kowhai Faults on geological timescales (Van Dissen & Yeats, 1991).

104 The details of the rupture pathway between the southern Humps–Hundalee fault  
105 system and the Kekerengu Fault are not well-resolved and two main pathways have been  
106 postulated. Firstly, the offshore route, from the Hundalee Fault to the Papatea Fault via  
107 mostly unmapped offshore thrust faults. This trajectory appears consistent with a range  
108 of observations including off-fault damage at the Papatea–Jordan Thrust–Kekerengu junc-  
109 tion (Klinger et al., 2018), kinematic (Holden et al., 2017) and dynamic rupture simu-  
110 lations (Ulrich et al., 2019), and tsunami modelling (Gusman et al., 2018; Bai et al., 2017).  
111 The second scenario involves rupture jumping from the Hundalee Fault to the Upper Kowhai  
112 Fault and onto the Jordan Thrust and Kekerengu Faults with limited slip on the inter-  
113 mediate Whites (Ando & Kaneko, 2018) and inferred Snowflake Spur Faults (Zinke et

---

<sup>1</sup> <https://www.geonet.org.nz/earthquake/technical/2016p858000> last accessed 24 April 2021

<sup>2</sup> <https://earthquake.usgs.gov/earthquakes/eventpage/us1000778i> last accessed 24 April 2021

114 al., 2019). The lack of resolution of the fault network and possible inter-connections at  
 115 depth inferred from surface observations alone mean that it remains unclear which sce-  
 116 nario actually occurred.

117 The rupture continued to propagate northwards onto the Needles Fault and other  
 118 faults in the Cape Campbell region before terminating near Cape Campbell itself (Kearse  
 119 et al., 2018), in the region of the 2013  $M_W$ 6.6 Cook Strait and Lake Grassmere earth-  
 120 quakes (Hamling et al., 2014). This northward rupture propagation resulted in strong  
 121 shaking in New Zealand’s capital city, Wellington (Kaiser et al., 2017; Bradley et al., 2017).  
 122 The reasons for rupture terminating near Cape Campbell, despite the availability of faults  
 123 straddling Cook Strait (Kearse et al., 2018), remains unclear. Dynamic rupture mod-  
 124 els (Ando & Kaneko, 2018; Ulrich et al., 2019) are able to capture most of the major fea-  
 125 tures of the Kaikōura rupture, including the absence of slip on the Hope Fault, maxi-  
 126 mum co-seismic offset, and the termination near Cape Campbell. However, how these  
 127 two models achieve termination at Cape Campbell differs: Ando and Kaneko (2018) ac-  
 128 counted for the termination by a c.  $10^\circ$  rotation in the prevailing stress field, which is in-  
 129 dicated by focal mechanism inversions using data from prior to the Cook Strait earth-  
 130 quakes (Balfour et al., 2005; Townsend et al., 2012). In contrast Ulrich et al. (2019) did  
 131 not invoke a stress rotation, and instead artificially reduce the stress on the Needles Fault.  
 132 It is also possible that the Cook Strait sequence invoked an as-yet unconstrained rota-  
 133 tion in the stress field, resulting in the pre-Kaikōura stress field differing from that used  
 134 by Ando and Kaneko (2018). Neither modelling study included the more favourably-oriented  
 135 faults that ruptured in the 2013 Cook Strait sequence.

136 In addition to the upper crustal faulting complexities, it remains unclear what role  
 137 the underlying subduction interface played in the Kaikōura earthquake (Hamling, 2020).  
 138 Lamb et al. (2018) suggested that the pattern of strain accumulation on the interface  
 139 can explain the diversity of crustal faulting, but it is not clear that the interface played  
 140 an active co-seismic role. Different models and data suggest differing contributions from  
 141 the subduction interface to the co-seismic moment budget of the Kaikōura earthquake.  
 142 Generally, models derived from regional data (e.g. Hamling et al., 2017; Gusman et al.,  
 143 2018; Holden et al., 2017) require negligible seismic moment on the underlying interface.  
 144 In contrast, studies using teleseismic data tend to favour more slip occurring on the sub-  
 145 duction interface (e.g. T. Wang et al., 2018; Bai et al., 2017). Whether the subduction  
 146 interface beneath the northern South Island can slip seismically is fundamentally impor-  
 147 tant to understanding seismic hazard in this populous region of New Zealand (Wallace  
 148 et al., 2018).

## 149 **1.2 Post-seismic Response**

150 Afterslip inferred using geodetic data from the Kaikōura fault system for the months  
 151 following the earthquake shows significant afterslip on the faults known to have ruptured  
 152 (Wallace et al., 2018; Mouslopoulou et al., 2019) accompanied by afterslip or triggered  
 153 slow-slip on the underlying subduction interface (Wallace et al., 2017; Yu et al., 2020;  
 154 Mouslopoulou et al., 2019) and triggered slow-slip in other regions of the Hikurangi mar-  
 155 ginal (Wallace et al., 2017). However, these models have used a relatively simple model  
 156 of crustal faulting that does not capture the spatial extent of aftershocks, in part due  
 157 to a lack of a dense, high-precision aftershock catalog.

158 Romanet and Ide (2019) observed tremor occurring prior to the Kaikōura earth-  
 159 quake, near the zone of mapped subduction interface afterslip, and suggested that the  
 160 tremor may be related to interface slip. However, it is also possible that the tremor lo-  
 161 cates on the downdip extent of faults in the Marlborough Fault Zone. Further work is  
 162 underway to better constrain these observations. Few aftershocks have yet been reliably  
 163 linked to slip on the subduction interface (Lanza et al., 2019).

164 The Kaikōura earthquake generated a significant and ongoing aftershock sequence  
 165 (Kaiser et al., 2017) and triggered earthquakes throughout New Zealand (Peng et al.,  
 166 2018; Yao et al., 2021). However, it was relatively unproductive compared to average statis-  
 167 tics for its magnitude (Chamberlain et al., 2020; Christophersen et al., 2017) resulting  
 168 in an over-estimation of aftershock rates early in the sequence when average aftershock  
 169 behaviour was used in forecasting<sup>3</sup>. This relatively low-productivity aftershock sequence  
 170 is in contrast to the similarly complex Ridgecrest earthquake, which was highly produc-  
 171 tive (Liu et al., 2019). Liu et al. (2019) suggested that the complexity of the Ridgecrest  
 172 earthquake may have promoted productivity due to strong stress concentrations around  
 173 fault step-overs. However, that explanation does not explain why the Kaikōura earth-  
 174 quake was relatively unproductive despite the involvement of significant stepovers and  
 175 presumably associated stress concentrations.

### 176 1.3 Unresolved Questions

177 Most models of co- and post-seismic slip around the Kaikōura earthquake have used  
 178 multi-fault models of fault ruptures, but these models have generally restricted the avail-  
 179 able faults to those with significant surface rupture, or simplifications thereof. The only  
 180 study that we are aware of that used aftershocks to better define the rupture geometry  
 181 focused on a small number of moment tensor solutions fixed at epicentres computed by  
 182 GeoNet (Cesca et al., 2017). We demonstrate in this paper that these GeoNet locations  
 183 are poorly constrained due to the use of the IASP91 (Kennett & Engdahl, 1991) 1D ve-  
 184 locity model (as also found by Yao et al., 2021; Lanza et al., 2019), rendering them too  
 185 inaccurate for use in defining fault structures.

186 Previous analysis of Kaikōura aftershocks (Lanza et al., 2019) has demonstrated  
 187 the diffuse nature of aftershocks around the step-over and Cape Campbell regions, which  
 188 suggests slip occurred on additional crustal faults. In this paper we expand on this af-  
 189 tershock catalog to explore the diversity of faulting around the faults that ruptured in  
 190 the Kaikōura earthquake, with the goal of shedding light on the pre-, co- and post-seismic  
 191 faulting processes. We particularly focus on several fundamental aspects of the rupture  
 192 that remain unresolved:

- 193 1. Rupture Initiation (Section 4.1): Where and how did the Kaikōura earthquake nu-  
 194 cleate and were there observable precursory signals?
- 195 2. Rupture Pathway (Section 4.2): What was the likely rupture pathway between  
 196 the southern fault system and the high-slip Kekerengu fault and how was this step-  
 197 over accommodated kinematically?
- 198 3. Subduction Interface (Section 4.3): What was the seismogenic role of the subduc-  
 199 tion interface beneath the known crustal fault ruptures of the Kaikōura earthquake?
- 200 4. Termination (Section 4.4): Why did the rupture terminate at Cape Campbell and  
 201 what was the significance of the previous 2013  $M_W$ 6.6 Cook Strait and Lake Grass-  
 202 mere earthquakes on this termination?
- 203 5. Post-seismic (Section 4.5): How did such co-seismic complexity affect post-seismic  
 204 afterslip?

## 205 2 Data and Methods

206 To obtain a more detailed picture of the fault geometry at depth, and the pre- and  
 207 post-seismic evolution of fault slip, we conducted a matched-filter search to generate a  
 208 more complete representation of the seismicity. We analysed >10 years of continuous data

---

<sup>3</sup> <https://www.geonet.org.nz/earthquake/forecast/kaikoura>, last accessed 22/01/2021

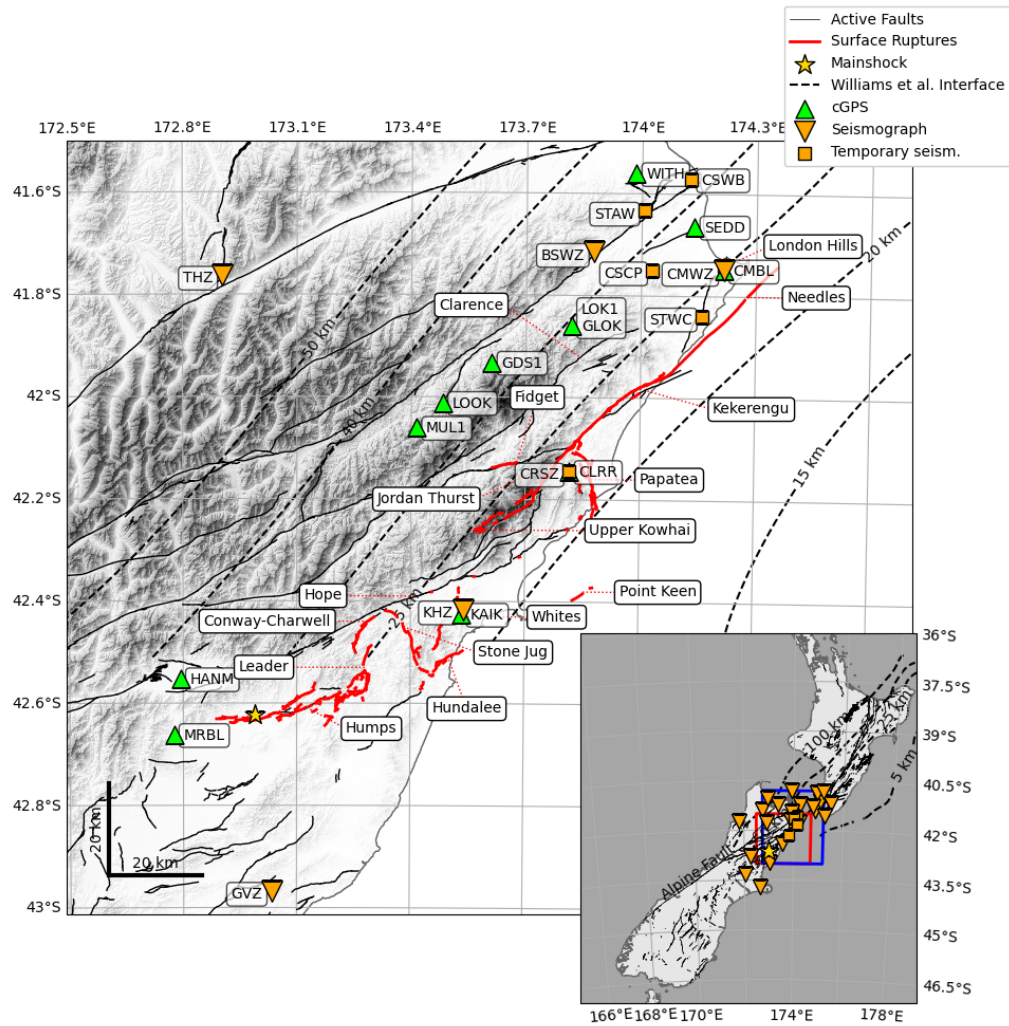


**Figure 1.** Main panel: GeoNet short-period and broadband seismographs (orange inverted triangles) used in this study for detection and picking, and temporary seismographs (orange squares) used solely for picking and continuous GNSS receivers (green triangles) active during the Kaikōura post-seismic period. Dashed lines mark the modelled subduction interface from C. A. Williams et al. (2013), and solid black lines mark faults of the NZ Active Fault Database (R. Langridge et al., 2016). Red lines mark the mapped surface ruptures of the Kaikōura earthquake (Clark et al., 2017), with names labelled. Inset: Regional setting of the Kaikōura region showing additional seismographs used for detection and location as inverted orange triangles. The location of the main panel is outlined as a red box, the region studied by Lanza et al. (2019) is shown as a blue box and solid and dashed lines are the active fault database and modelled subduction interface respectively.

209 using earthquakes that occurred on the faults that ruptured co- and post-seismically in  
 210 the Kaikōura earthquake as template events.

211 We used the catalog of 2,654 aftershocks and the mainshock picked and located by  
 212 Lanza et al. (2019) as template events to provide a methodologically consistent set of  
 213 phase-picks. This catalog includes every event of  $M_L \geq 3$  cataloged by GeoNet that  
 214 occurred between 13 November 2016 and 13 May 2017 (UTC) in a rectangular region  
 215 between latitudes  $-43.00^\circ$  and  $-40.80^\circ$  and longitudes  $172.75^\circ$  and  $175.20^\circ$ , apart from 110  
 216 earthquakes that had poorly constrained depths. We previously attempted to use the  
 217 GeoNet catalog directly to construct templates but found that the phase pick-quality  
 218 was too variable, and the paucity of S-picks hindered our detection capability: the re-  
 219 sulting catalog contained excessive false detections. The Lanza et al. (2019) catalog con-  
 220 tains the dominant, moderate-to-large magnitude seismicity recorded in the seven months  
 221 following the Kaikōura mainshock.

222 We constructed templates using data from 21 GeoNet broadband and short-period  
 223 seismographs (Figure 1). We excluded strong-motion instruments from our analysis due  
 224 to their variable timing quality (S. Bannister pers. comm.). Note that these stations were  
 225 included in the analysis of Lanza et al. (2019) and may have degraded location quality  
 226 in this prior work. We did not include temporary stations (e.g. from the STREWN net-  
 227 work, as analysed by Lanza et al. (2019)) in our detection effort to exclude bias in de-  
 228 tectations arising from variations in network geometry and station density.

229 Templates were made using EQcorrscan (Chamberlain et al., 2018). Continuous  
 230 day-long data were detrended, resampled in the frequency-domain to 30.0 Hz to reduce  
 231 computational load, filtered using a 4th-order Butterworth bandpass filter between 1.5  
 232 and 12 Hz, and trimmed to 4 s length around the P and S phase-picks on the vertical and  
 233 horizontal channels respectively. We tested a range of filters and template lengths and  
 234 found that using a higher low-cut frequency resulted in additional false detections likely  
 235 related to correlations with high-frequency noise, whereas using a lower low-cut frequency  
 236 resulted in a degradation of correlations with true detections and an increase in back-  
 237 ground (e.g. noise) correlation sums. Increasing the length of templates resulted in ex-  
 238 cessive phase-overlap and compromised our ability to conduct later phase-picking anal-  
 239 ysis of detections. We removed channels with a signal-to-noise ratio less than four, where  
 240 we computed signal-to-noise ratio using the ratio of the maximum amplitude in the tem-  
 241 plate to the root-mean-squared amplitude of 100 s of pre-template noise. Finally we re-  
 242 moved templates containing data from fewer than five stations, leaving a set of 2,584 tem-  
 243 plates.

244 We computed detections between 1 January 2009 and 1 January 2020 using the EQ-  
 245 corrscan package (Chamberlain et al., 2018) which computes the network-wide stack of  
 246 the normalized cross-correlation between template waveforms and continuous data across  
 247 multiple channels. We used the efficient FFTW (Fastest Fourier Transform in the West  
 248 Frigo and Johnson (1998)) backend that implements the chunked-correlation algorithm  
 249 of Senobari et al. (2019), and the FMF (Fast-Matched-Filter Beaucé et al. (2018)) GPU-  
 250 based routine when a GPU was available. Note that in compiling this catalog we imple-  
 251 mented full normalization in the FMF code to ensure compatibility with other correla-  
 252 tions<sup>4</sup>.

253 Detections were made when the summed correlations exceeded  $10\times$  the median ab-  
 254 solute deviation of the day-long stack of correlations, and had at least an average nor-  
 255 malized correlation above 0.15. To cope with degraded correlations at the end of cor-  
 256 relation epochs (in this case days) due to the delay-and-stack approach taken to com-  
 257 pute the summed correlations, we overlapped each day of correlation by the maximum

---

<sup>4</sup> Full-normalization in FMF: [https://github.com/beridel/fast\\_matched\\_filter/pull/38](https://github.com/beridel/fast_matched_filter/pull/38)

258 moveout in the templates. Detections from individual templates were required to be at  
 259 least 4 s apart. To remove duplicate detections (e.g. detections of the same event by dif-  
 260 ferent templates), we retained only the detections with the highest average correlation  
 261 if multiple detections occurred within 1 s of each other.

262 To enable location of the detected events and further remove false detections we  
 263 computed cross-correlation derived phase-picks, following the methodology outlined by  
 264 Warren-Smith et al. (2017). For each detection, the relevant channel of the template and  
 265 continuous data were correlated in a short window of  $\pm 0.5$  s around the assumed pick-  
 266 time based on a time-shifted version of the template phase-pick. A pick was made at the  
 267 maximum of this 1 s-long correlogram, if the maximum normalized correlation exceeded  
 268 0.4. Following this step, detections with picks on fewer than five stations were removed.  
 269 This provided a catalog of 33,343 events comprising 899,460 phase-picks. In this pick-  
 270 ing step we incorporated the four temporary STREWN stations around Cape Campbell,  
 271 and GeoNet station CRSZ, deployed after the Kaikōura earthquake, to enhance our lo-  
 272 cations, without biasing our detections.

273 Because most of our detections were made during the active aftershock sequence  
 274 of the Kaikōura earthquake, some of the correlation picks we made were associated with  
 275 the wrong event due to overlapping events from different parts of the aftershock region.  
 276 To combat this we undertook an additional quality-control step in which, for each event,  
 277 we located the event using HYPOCENTER (Lienert & Havskov, 1995) and the 1D ve-  
 278 locity model of Okada et al. (2019). If the root-mean-squared (RMS) travel-time resid-  
 279 ual of the location exceeded 1 s the pick with the highest residual was removed and the  
 280 event located again. We repeated this process until either the RMS fell below 1 s, or picks  
 281 from fewer than five stations remained. If the events RMS did not drop below 1 s with  
 282 more than five stations, the event was discarded. This removed 30 events leaving us a  
 283 total of 33,328 events and 896,727 phase picks.

284 We located the detected earthquakes using the NonLinLoc software of Lomax et  
 285 al. (2000) and the New Zealand-wide 3D (NZ3D) velocity model of Eberhart-Phillips et  
 286 al. (2017), version 2.2, which includes the updated tomography around the Cook Strait  
 287 region conducted by Henrys et al. (2020). We note that the issues encountered by Lanza  
 288 et al. (2019) in using NonLinLoc were rectified here by changing a flag in the NonLin-  
 289 Loc Grid2Time3D source-code. We also tested using SIMUL2014 (Eberhart-Phillips &  
 290 Bannister, 2015) and found that the fit to the data was degraded compared to our Non-  
 291 LinLoc locations. We suspect that this reduced quality is because our events frequently  
 292 contain S-picks without a corresponding P-pick, which SIMUL2014 cannot use. This is  
 293 because S-phases usually correlate better than P-phases due to their high amplitudes.  
 294 We were able to locate all events, but only 32,939 events are considered here because 389  
 295 occurred outside the study region (Figure 2).

296 Following this location step, we made automatic amplitude picks for all events and  
 297 used these to compute local magnitudes. We used the EQcorrscan (Chamberlain et al.,  
 298 2018) amplitude-picking routines which pick half the maximum peak-to-trough ampli-  
 299 tude on a filtered, Wood-Anderson-simulated trace and correct for the applied filter. Com-  
 300 parison of these automatic picks with GeoNet amplitude picks for similar events (both  
 301 those within the template set and not in the template set) shows good agreement. We  
 302 then computed local magnitudes by inverting for a local magnitude scale that maps to  
 303 moment magnitudes, following the methodology of (Michailos et al., 2019), taken from  
 304 the moment tensor catalog maintained by GeoNet and based on the work of Ristau (2013).

305 We subsequently undertook relative relocation of all earthquakes using the Grow-  
 306 Clust software (Trugman & Shearer, 2017) and HypoDD (version 2.1b) (Waldhauser &  
 307 Ellsworth, 2000). For GrowClust we used an average 1D velocity model extracted from  
 308 the NZ3D velocity model (between 72–110 km in X and –100–80 km in Y in the coordi-  
 309 nate system of Eberhart-Phillips and Bannister (2015), Supplementary Table S1) used

310 for initial location. For HypoDD we used the NZ3D model version 2.2 (Henry et al., 2020;  
 311 Eberhart-Phillips & Bannister, 2015). We found little difference between the two loca-  
 312 tion methods, and so report the GrowClust locations here because they provide robust,  
 313 bootstrapped uncertainties (Trugman & Shearer, 2017). We were able to relocate 27,431  
 314 earthquakes in total.

315 Finally, we computed first-motion-derived focal mechanism solutions for template  
 316 events. To compute template focal mechanisms we undertook manual polarity deter-  
 317 mination of the automatically determined P arrivals from Lanza et al. (2019). We in-  
 318 cluded stations from the STREWN network, and strong-motion stations in the GeoNet  
 319 network (station locations are plotted in Supplementary Figure S8), but note that we  
 320 did not use the timing of these phase arrivals in our location calculations. We then in-  
 321 verted for the best-fitting focal mechanisms of all template events with polarity picks at  
 322 more than 8 stations ( $n=1,754$ ) using the Bayesian algorithm developed by Walsh et al.  
 323 (2009). We used our NonLinLoc derived location estimates and uncertainties to com-  
 324 pute takeoff angle and azimuth posterior density functions.

### 325 **3 Results**

326 We detected and located 33,328 earthquakes that occurred between 1 January 2009  
 327 and 1 January 2020 associated with the regions active during the aftershock sequence  
 328 of the 2016 Kaikōura M7.8 earthquake. Of these earthquakes, we were able to compute  
 329 precise relative relocations for a suite of 27,431 earthquakes (Figure 2). Our NonLinLoc  
 330 locations have median 68% confidence uncertainties of between 1.8 km and 3.0 km (min-  
 331 imum and maximum confidence ellipsoid lengths) and 2.8 km in depth (Supplementary  
 332 Figure S6). Our GrowClust relocations have median relative uncertainties of 0.2 km in  
 333 horizontal and depth directions.

334 As found by Lanza et al. (2019), but not by GeoNet, our hypocentre location for  
 335 the Kaikōura mainshock (latitude  $-42.624$ , longitude  $172.989$ , depth: 12.5 km) lies al-  
 336 most directly beneath the Humps Fault, about 8.2 km NNW from the GeoNet location  
 337 (beyond the bounds of uncertainties of either location) and c. 2 km north of the location  
 338 obtained by Nicol et al. (2018). We were not able to relocate the mainshock hypocen-  
 339 tre (using GrowClust or HypoDD) due to the complexity and clipping of the waveforms  
 340 and resulting low correlations with other events. This mis-location by GeoNet is likely  
 341 due to the use of an inappropriate velocity model (ISAP91: <https://www.geonet.org.nz/earthquake/technical/2016-01-13-14-15-16-17-18-19-20-21-22-23-24-25-26-27-28-29-30-31-32-33-34-35-36-37-38-39-40-41-42-43-44-45-46-47-48-49-50-51-52-53-54-55-56-57-58-59-60-61-62-63-64-65-66-67-68-69-70-71-72-73-74-75-76-77-78-79-80-81-82-83-84-85-86-87-88-89-90-91-92-93-94-95-96-97-98-99-100>  
 342 last accessed September 7 2020). We discuss the variation in hypocentre location fur-  
 343 ther in Section 4.1.

344 We obtain magnitudes ranging from 0.2–6.3 (Figure 3). We note that the maxi-  
 345 mum magnitude of 6.3 was computed for the  $M_W$  7.8 mainshock, which is beyond the  
 346 range at which we would expect reliable amplitude-based local magnitudes (see Supple-  
 347 mentary Figure S5). The largest aftershock magnitude we calculated is  $M_L$  5.9 30 minutes  
 348 after the mainshock, for which GeoNet provide a magnitude of  $M_L$  6.2. In general our  
 349 local magnitude scale gives lower magnitudes than GeoNet at high magnitudes (Supple-  
 350 mentary Figure S5). We were unable to calculate magnitudes for 50 earthquakes due to  
 351 insufficient amplitude picks of sufficient quality. The completeness of our catalog is strongly  
 352 variable in time: as noted by Hainzl (2016), during periods of high-rate seismicity the  
 353 magnitude of completeness increases, and we observe this after the Kaikōura mainshock.  
 354 Before and within a few months after the mainshock, our magnitude of completeness is  
 355 around  $M_L$  1.2, however in the hours after the mainshock the completeness becomes as  
 356 elevated as  $M_L$  3.8 (Figure 3). One of the main causes of elevated completeness, despite  
 357 the ability of the matched-filter method to detect earthquakes with overlapping wave-  
 358 forms, is the restriction in our workflow to only detect events separated by at least 1 s.

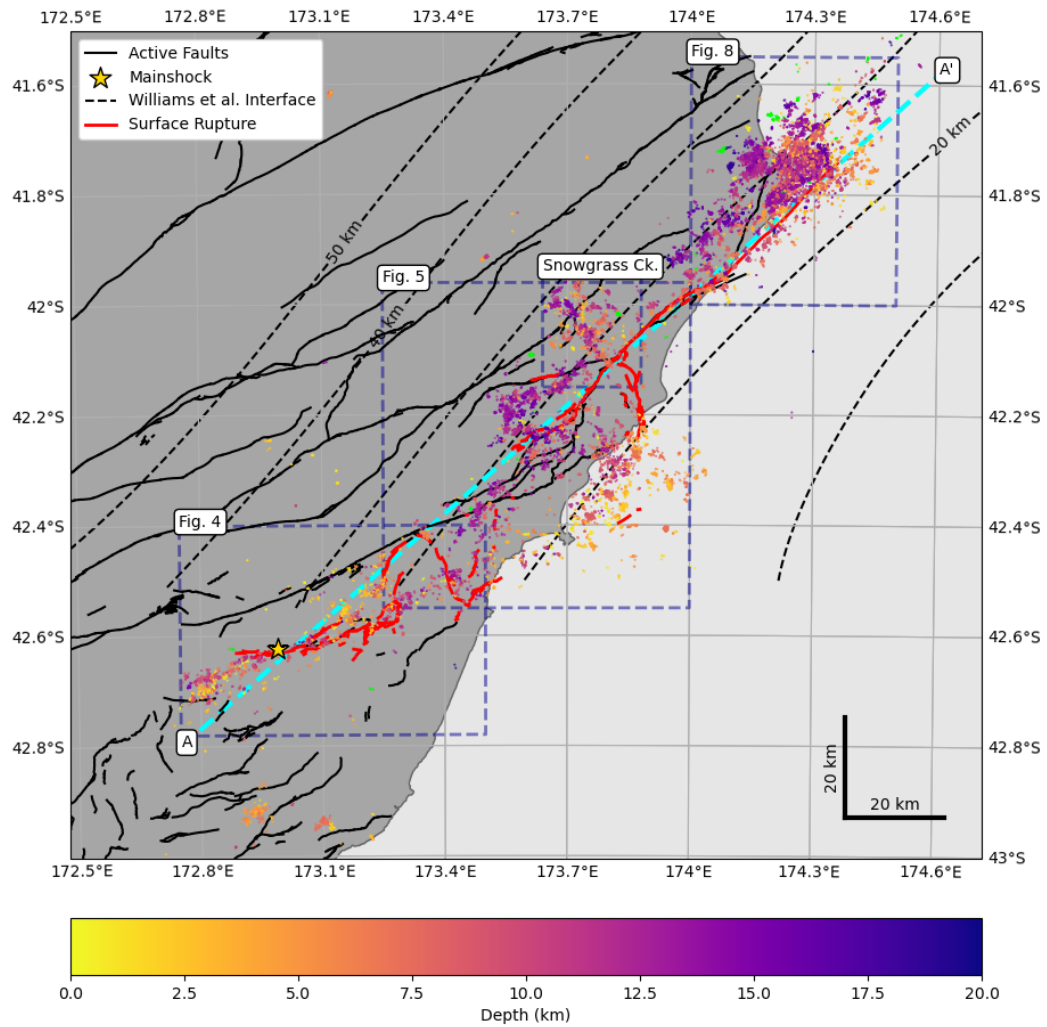


**Figure 2.** Earthquakes on and around the faults (red lines) that ruptured in the Kaikōura earthquake plotted as circles coloured by depth. Earthquakes deeper than 20 km are plotted in green. Dashed contours mark the depth to the modelled subduction interface (C. A. Williams et al., 2013). The dashed cyan line, labelled A-A' is the cross-section line shown in Figure 7. Dashed dark blue boxes mark the bounds of the relevant figures. The gold star marks the mainshock hypocentre computed here.

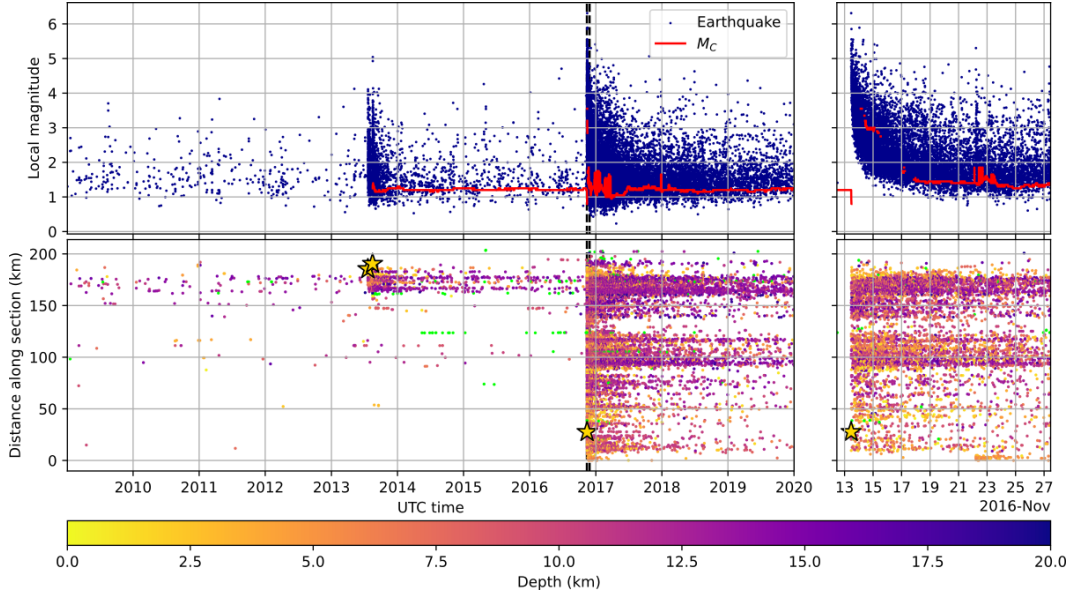


**Figure 3.** Upper panel: Local magnitudes for all earthquakes in our catalog (blue) and magnitude of completeness computed by goodness-of-fit (Wiemer, Stefan and Wyss, Max, 2000) (red). Magnitude of completeness was computed using a sliding window of 1,000 events. Magnitude of completeness is only shown when at-least 300 magnitudes were above the best fitting completeness, and the fit was above 98%. Lower panel: Earthquakes projected onto the A-A' cross-section (Figure 2), and plotted against origin-time. Earthquakes are coloured by depth. Earthquakes deeper than 20 km are plotted in green and the grey ellipse outlines the deep normal-faulting sequence discussed in the text. The Lake Grassmere, Cook Strait and Kaikōura earthquakes are plotted as gold stars. Right panels show zoomed in views of the two weeks following the Kaikōura mainshock, marked as vertical dashed black lines in the left panels.

359 The vast majority of earthquakes in our catalog are aftershocks of the Kaikōura  
 360 earthquake (30,652 events, or 92%, occurred after the mainshock). The earliest after-  
 361 shock we detect occurred 2 minutes and 48 s after the mainshock origin time, approxi-  
 362 mately 45–65 s after the completion of the mainshock rupture (Holden et al., 2017). How-  
 363 ever our catalog also includes aftershocks of the Cook Strait earthquakes, with 2,326 earth-  
 364 quakes between the start of the Cook Strait sequence on the 18th of July 2013 and the  
 365 Kaikōura mainshock. Some events in our catalog appear to be associated with failure  
 366 within the subducted plate. The sequence of earthquakes visible in Figure 3 at c. 125 km  
 367 along the section occur at c. 25 km depth and have focal mechanisms consistent with normal-  
 368 faulting in the subducted slab. Interestingly this family of earthquakes culminated in a  
 369 sequence of eight earthquakes in the seven days prior to the Kaikōura mainshock. We  
 370 also detect limited earthquakes associated with slip on the subduction interface made  
 371 by templates representing likely interface events reported by Lanza et al. (2019) near Cape  
 372 Campbell. Most (28,768 or 86% of absolute locations and of 24,568 or 90% relative re-  
 373 locations) of our earthquakes are found to have been shallower than 15 km.

## 374 4 Discussion

375 This updated and expanded catalog of earthquakes on and surrounding the faults  
 376 that ruptured in the Kaikōura earthquake serves as the basis to re-evaluate some of the  
 377 outstanding questions regarding this complex earthquake. Here we discuss the key ques-  
 378 tions outlined previously and highlight some key fault structures that have previously  
 379 been poorly resolved or unknown.

### 380 4.1 Rupture Initiation

381 Multiple hypocentre locations for the Kaikōura earthquake are now available and,  
 382 as demonstrated by Nicol et al. (2018), there is some inconsistency between them. In our  
 383 locations we find that the mainshock hypocentre locates almost directly beneath the sur-  
 384 face trace of the Humps Fault, at a depth of  $12.5 \pm 5.8$  km (Figure 4). The first-motion-  
 385 derived focal mechanism of the mainshock that we construct here (strike/dip/rake of  $245^\circ/80^\circ/175^\circ$ )  
 386 is consistent with dextral slip on a steeply dipping plane similar to the strike of the Humps  
 387 Fault. A Gaussian fit to the NonLinLoc uncertainties at the  $1\sigma$  level provides a horizon-  
 388 tal uncertainty ellipse oriented at  $96^\circ$  with a maximum length of 2.3 km and minimum  
 389 length of 1.8 km. Our location is slightly different (but within uncertainty) from that of  
 390 the previous solution of Lanza et al. (2019), whose phase picks we use here, and notably  
 391 different from the Geonet location that does not place the hypocentre on the Humps Fault.  
 392 The GeoNet hypocentre could indicate that an initial rupture on a separate fault to the  
 393 south occurred, which subsequently triggered slip on the Humps Fault as suggested by  
 394 Ando and Kaneko (2018) to explain some of the mismatch in the initial rupture speed  
 395 between their model and observations. However, we are confident that the rupture did  
 396 in fact nucleate on the Humps Fault, and discuss possible causes of the discrepancies in  
 397 locations below.

398 In this work we have not used picks on the strong-motion sites with known tim-  
 399 ing problems. We also use an updated velocity model, and a different location method  
 400 compared to Lanza et al. (2019). When we use the same location method (using the soft-  
 401 ware SIMUL) and/or use the same velocity model as Lanza et al. (2019), we obtain a  
 402 similar result to our preferred solution, suggesting that the main source of error in the  
 403 previous location of Lanza et al. (2019) was from the inclusion of picks from sites with  
 404 problematic timing.

405 The GeoNet preferred location for the mainshock hypocentre (at the time of writ-  
 406 ing this, 24 April 2021, was at  $-42.693^\circ$  N,  $173.022^\circ$  E and 15.11 km depth) lies 8.2 km to  
 407 the south of our location, beyond the combined uncertainties in our location and the quoted  
 408 horizontal uncertainty in the GeoNet location (2.3 km in latitude and 3.4 km in longi-

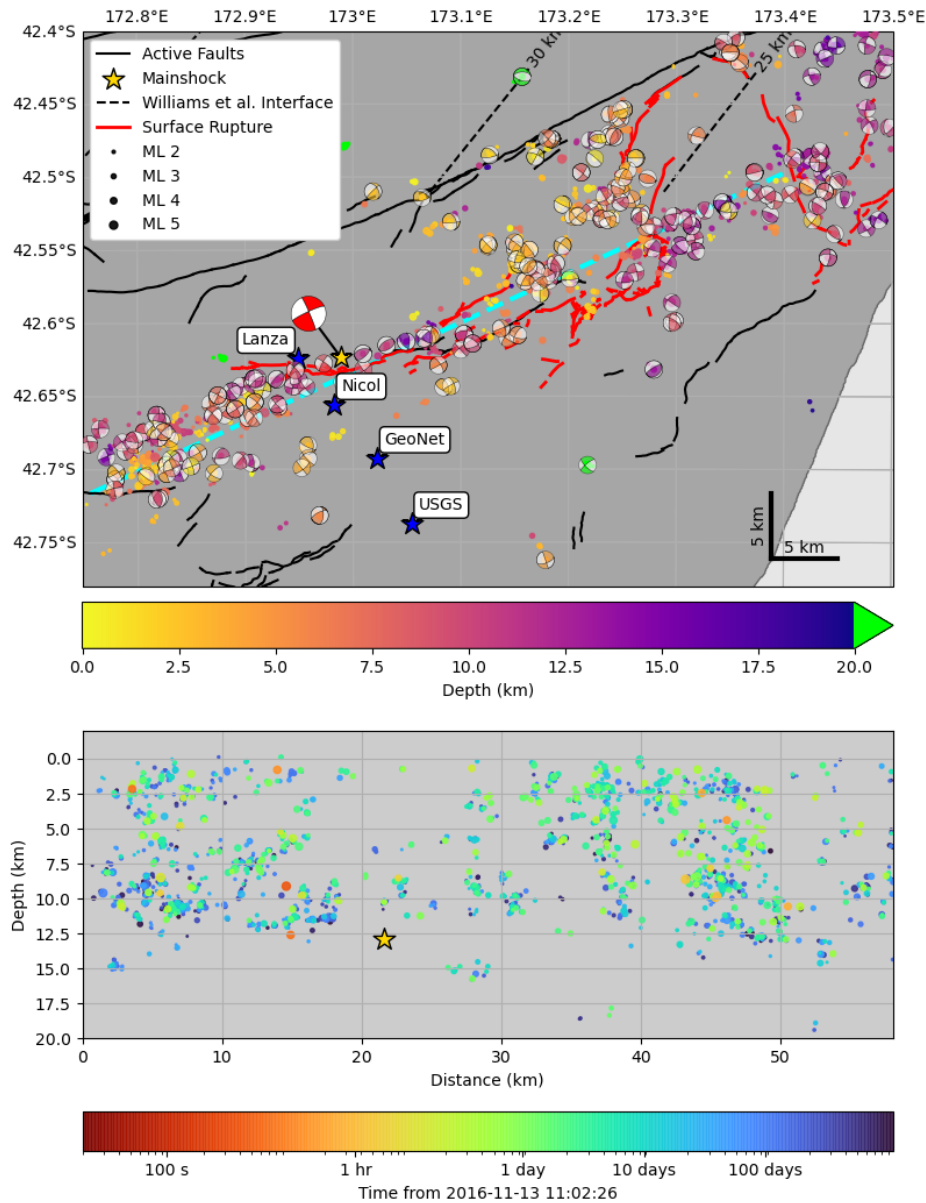


**Figure 4.** Nucleation region of the Kaikōura earthquake. Upper panel: map of relocated earthquakes (circles coloured by depth and scaled by magnitude) and focal mechanisms of template events, coloured by depth. Earthquakes deeper than 20 km are plotted in green. Mainshock location is marked by a star: note that this is an absolute location rather than a relocation for reasons explained in the text. The first-motion derived focal mechanism of the mainshock is shown in red. Alternative mainshock locations are plotted as blue stars and labelled as Lanza, Nicol, GeoNet and USGS for the Lanza et al. (2019), Nicol et al. (2018) GeoNet and USGS solutions respectively. Mapped surface ruptures are plotted as red lines, and other faults of the NZ active faults database are plotted in black. Dashed black contours mark the modelled subduction interface from C. A. Williams et al. (2013). The dashed cyan line shows the cross-section line plotted in the lower panel. Lower panel: Cross-section (SW to NE) of relocated hypocentres projected onto the cyan line in the upper panel. Earthquakes are coloured by time since 30s prior to mainshock, note that the colourscale is logarithmic. Earthquakes are scaled by magnitude. The star marks the absolute location of the mainshock.

409 tude). The GeoNet solution is computed using the IASP91 (Kennett & Engdahl, 1991)  
 410 global 1D velocity model and the LOCSAT location program (Bratt & Nagy, 1991). When  
 411 we locate the mainshock using the GeoNet pick times in NonLinLoc using the NZ3D 2.2  
 412 velocity model used here we obtain a similar location to our location (within uncertainty).  
 413 We suggest that the use of the global 1D velocity model is inappropriate for accurate  
 414 location of crustal seismicity in New Zealand, and results in incorrect locations and un-  
 415 der estimated location uncertainties, as also shown in central North Island by Illsley-Kemp  
 416 et al. (2021). Similar issues are likely to apply to other location solutions for the Kaikōura  
 417 mainshock that do not use an appropriate velocity model.

418 The location computed by Nicol et al. (2018) is within the uncertainty of our loca-  
 419 tion, and was computed using a similar method to that used here. However, the af-  
 420 tershock relocations computed by Nicol et al. (2018) use GeoNet locations as starting  
 421 locations, which are inaccurate due to the use of the IASP91 velocity model. As such,  
 422 relocation from these inaccurate starting locations is the likely cause of difference between  
 423 the relocations of Nicol et al. (2018) and those presented here, which here delineate a  
 424 nearly vertical structure consistent with our mainshock focal mechanism. The south-dipping  
 425 lineation extending through the subduction interface shown by Nicol et al. (2018) is not  
 426 visible in our relocations, probably due to more robust starting locations used here.

427 We note that a foreshock *c.* 7 s prior to the mainshock (Supplementary Figure S1)  
 428 may also have contributed to inaccuracies in mainshock location: if picks were made on  
 429 the much smaller foreshock P-phases for the four GeoNet stations that they are visible  
 430 on then these arrival times would bias the location. This foreshock is located close to  
 431 the mainshock, but the mainshock obscures the S-phase on most stations and the P-phase  
 432 is only visible on four stations due to the size of the foreshock, and the resulting loca-  
 433 tion we obtain has high uncertainties. We did not detect this foreshock with our matched-  
 434 filter detector due to the poor signal on most stations, and it is therefore not included  
 435 in our catalog.

436 In summary, our more accurate mainshock location and focal mechanism confirm  
 437 that the Kaikōura earthquake most likely nucleated as a dextral strike-slip rupture of  
 438 the Humps Fault, and confirm that the Humps Fault here is steeply dipping (*c.* 80°) to  
 439 the North. This suggests that off-fault triggering did not play a strong role in the nu-  
 440 cleation of the Kaikōura earthquake, and other factors must be the cause of the early  
 441 long-duration release of seismic energy. Ulrich et al. (2019) were able to reproduce the  
 442 slow initial phase of the rupture through the Humps–Hundalee system in their dynamic  
 443 rupture simulation. Finally, it is worth noting that any seismic backprojections that com-  
 444 pute the location of high-frequency radiation sources relative to the mainshock may be  
 445 biased by the use of inaccurate hypocentres (e.g. Tan et al., 2019; D. Wang et al., 2018).

446 We do not observe precursory seismicity in our catalog aside from the foreshock  
 447 approximately 7 s prior to the mainshock which we did not detect by matched-filter and  
 448 is not included in our final catalog. This includes no seismicity in the epicentral region  
 449 following any of the 2010 Darfield earthquake, 2011 Christchurch earthquakes, or the 2013  
 450 Cook Strait sequence, which are likely to have induced dynamic stress changes in the epi-  
 451 central region of the Kaikōura earthquake. We attempted to run a focused matched-filter  
 452 search using GeoNet data and the 7 s foreshock as a template, but this did not make any  
 453 further reliable detections. We note that our catalog is likely biased by being constructed  
 454 using only aftershocks as templates, and the presence of at least one visible foreshock  
 455 should motivate further analysis of foreshock activity here.

## 456 4.2 Rupture Pathway

457 The Kaikōura earthquake involved substantial rupture ( $>1.5$  m surface slip) of at  
 458 least 13 faults (Litchfield et al., 2018). Initial observations suggested that large stepovers  
 459 (up to 20 km), particularly between the southern faults (Humps–Hundalee system) and

460 the high slip Kekerengu Fault, were present (Kaiser et al., 2017; Hamling et al., 2017).  
461 Such large stepovers commonly correspond to rupture termination points (Wesnousky,  
462 2006; Harris et al., 1991). More recently, additional faults, including the Point Keen or  
463 other offshore reverse faults, and/or links between the Hundalee and Jordan Thrust/Upper  
464 Kowhai Faults (via the Leader and Whites Faults) have been postulated to explain the  
465 rupture sequence (e.g. Ando & Kaneko, 2018; Zinke et al., 2019). In particular, the dy-  
466 namic rupture model of Ando and Kaneko (2018) has rupture propagating from the Hun-  
467 dalee Fault to the Upper Kowhai and Jordan Thrust Faults with limited slip on the link-  
468 ing Whites Fault (Figure 6), and suggests that this step-over was accommodated mostly  
469 by transient dynamic stresses or elastic waves. In contrast, the dynamic rupture model  
470 of Ulrich et al. (2019) has rupture propagating from the Hundalee Fault onto the offshore  
471 reverse faults before triggering slip on the Papatea Fault, which then caused rupture of  
472 the Jordan Thrust and Kekerengu Faults.

473 Although we do not have direct co-seismic evidence in our catalog of the rupture  
474 pathway, our earthquake locations help to illuminate the structure of these linking faults  
475 at depth (Figure 5). Two key faults emerge: (1) an offshore, dominantly reverse, struc-  
476 ture similar to the Point Keen Fault modelled by Ulrich et al. (2019); Hamling et al. (2017)  
477 and (2) a previously unidentified strike-slip, near-vertical structure linking the Papatea-  
478 Jordan Thrust-Kekerengu-Fidget junction to the inland, unruptured Clarence Fault. We  
479 herein refer to this second new fault as the Snowgrass Creek Fault, named after a nearby  
480 stream. The Snowgrass Creek Fault strikes approximately  $140^\circ$ , has a near vertical dip,  
481 and a surface length of approximately 12 km. Note that this fault is not associated with  
482 any reported surface rupture. There is also a continuous trend of earthquake locations  
483 spanning the gap between the southern fault system and the Jordan Thrust, suggest-  
484 ing that either the offshore route, via the offshore thrust system, or the onshore route,  
485 via the Whites Fault are viable options for rupture propagation.

486 Several key observations provide further constraints on the most likely rupture route  
487 for the Kaikōura earthquake, principally the occurrence of a small, localised tsunami (Gusman  
488 et al., 2018), and the inverted motion of the Jordan Thrust, which hosted normal motion  
489 rather than the reverse motion, as would be expected from the geological record (Howell  
490 et al., 2020; Van Dissen & Yeats, 1991). We propose that these two factors, alongside  
491 our observation that offshore thrust faulting spans the gap between the Hundalee Fault  
492 and the Papatea Fault, require that the earthquake propagated via the offshore route  
493 (Figure 6). In addition the observation of a tsunami requires some co-seismic offshore  
494 deformation which would be provided by offshore thrust faulting (Gusman et al., 2018),  
495 and the normal (inverted) sense of slip on the Jordan Thrust Fault can be explained by  
496 our preferred model. This is in agreement with recent modelling studies by Ulrich et al.  
497 (2019) and Klinger et al. (2018).

498 In our preferred rupture scenario we suggest that the offshore thrust fault (or faults,  
499 here labelled as the Point Keen Fault for consistency, despite the opposite sense of slip  
500 compared to the geologically recognised Point Keen Fault (Litchfield et al., 2018)), the  
501 Papatea Fault, and extending into the newly discovered Snowgrass Creek Fault acted  
502 as one thrust block with a sinistral north-western edge (Figure 6). Within this thrust  
503 block, the normal motion of the usually reverse Jordan Thrust Fault occurs as a con-  
504 sequence of the eastward motion of eastern side of the block (normally the footwall). In  
505 other words, the coastal side of the Jordan Thrust is extended seawards relative to the  
506 pinned inland side resulting in normal motion.

507 This scenario can also help explain the high slip on the Papatea Fault. In this sce-  
508 nario, the Papatea Fault sits at the corner between dominantly thrust motion offshore,  
509 to dominantly sinistral-normal oblique motion onshore on the Snowgrass Creek Fault.  
510 Not only does this scenario provide additional fault length for the combined Papatea-  
511 Snowgrass Creek-Point Keen Fault system, meaning that co-seismic displacements scale  
512 more consistently with fault length, but also that the Papatea Fault acts in a similar style

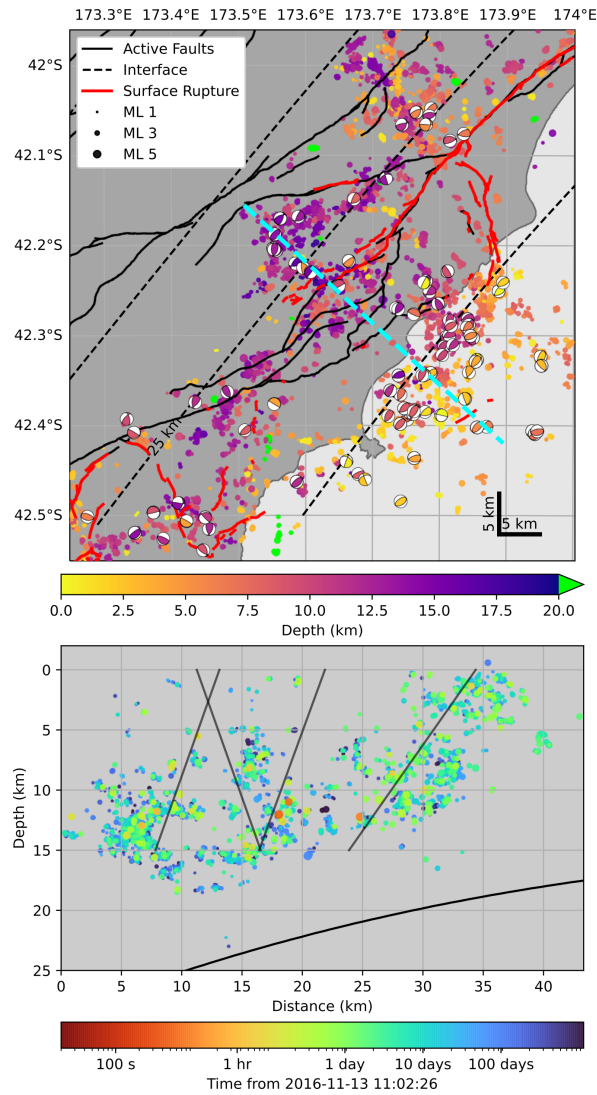


**Figure 5.** Earthquake locations around the transition from southern/epicentral faults to the Keckerengu fault. Top: map view of relocated earthquakes plotted as circles coloured by depth and scaled by magnitude. Earthquakes deeper than 20 km are plotted in green. Thrust focal mechanisms ( $45^\circ < \text{rake} < 135^\circ$ ) for template events are also plotted, coloured by depth. Active faults are plotted in black, and faults with known surface rupture during the Kaikōura earthquake are plotted in red. Black dashed contours mark the depth to the interface model of C. A. Williams et al. (2013). The cyan dashed line marks the cross-section line shown in the lower panel. The green solid line marks the inferred location of the newly identified Snowgrass Creek fault (labelled). Note that the surface dip of the Clarence Fault is c.  $70^\circ$  NW (Rattenbury & Isaac, 2012), and the Snowgrass Creek fault appears to terminate at the Clarence Fault at depth. Bottom: Cross-section perpendicular to the dominant strike of reverse focal mechanisms. Earthquakes within 7.5 km of the cross-section are projected onto the line. Solid straight lines mark the locations and dips of cross-section intersecting faults from Litchfield et al. (2018). The solid curved line at depth marks the subduction interface model of C. A. Williams et al. (2013). Note that the broad cluster of earthquakes at the down-dip end of the Upper Kowhai Fault is likely associated with projecting earthquakes on a fault striking obliquely to the cross-section. Similarly, our preferred arcuate geometry of offshore thrusting, and variable dip provides an explanation for the broad region of earthquakes below the inferred Point Keen Fault.

513 to a restraining bend, e.g. with large co-seismic strain exceeding the long-term accumu-  
 514 lated elastic strain, which other authors have suggested is insufficient to explain the slip  
 515 amplitude on the Papatea Fault (e.g. Diederichs et al., 2019).

516 We use the same equations, converted to SI units, as R. M. Langridge et al. (2018),  
 517 after Stirling et al. (2012), namely:

$$M_W = 2/3 \log W + 4/3 \log L - 1.82, \quad (1)$$

518 where  $W$  is fault width and  $L$  is fault length, both in meters, and

$$M_0 = \mu L W D, \quad (2)$$

519 where  $M_0$  is the seismic moment in N·m,  $\mu$  is the shear modulus, which Stirling et al.  
 520 (2012) assume to be  $3 \times 10^{10}$  Pa,  $L$  and  $W$  are as before, and  $D$  is the single-event dis-  
 521 placement in meters.  $M_0$  is calculated using:

$$\log M_0 = 9.05 + 1.5 M_W. \quad (3)$$

522 This way, we are able to estimate single-event displacements for various fault combina-  
 523 tions. We deduce that R. M. Langridge et al. (2018) adopted a fault width of 18.5 km  
 524 based on the magnitude they compute. Using this fault width and a combination of the  
 525 Papatea and Snowgrass Creek faults (which adds approximately 15 km to the length when  
 526 incorporating the dip of the Clarence Fault and hence additional length of the Snowgrass  
 527 Creek Fault at depth) we find a single-event displacement of 2.3 m. Incorporating the  
 528 Point Keen Fault in our preferred geometry results in an 83 km total length and aver-  
 529 age displacement of 5.8 m. Finally, including the section of the Hundalee Fault between  
 530 the coast and the Stone Jug Fault increases the length to 93 km and slip to 6.5 m. The  
 531 average net slip on the Papatea Fault was measured to be  $6.4 \pm 0.2$  (R. M. Langridge et  
 532 al., 2018), reinforcing our proposed combined fault system explanation.

533 The existence of the Snowgrass Creek Fault also helps to explain the drop in slip  
 534 across the Kekerengu-Jordan Thrust junction, despite the similar strikes of these two faults.  
 535 A simple model of this junction is that of a quadruple junction between the Jordan Thrust,  
 536 Papatea, Kekerengu and Snowgrass Creek Faults (discounting the Fidget Fault that has  
 537 mapped surface rupture away from the junction, but not nearby (Litchfield et al., 2018)).  
 538 By averaging the InSAR derived coseismic displacement field (Hamling, 2020) in blocks  
 539 around the fault system (see Supplementary Figures S2 and S3) we estimate the strike-  
 540 parallel and perpendicular components of motion on the Snowgrass Creek to be 1.3 m  
 541 sinistral and 3.4 m of extension. The resulting sinistral transtensional motion is consis-  
 542 tent with the dominant aftershock focal mechanisms (Supplementary Figure S8). The  
 543 strong change in the InSAR-derived North-South displacement field aligns with the strike  
 544 of the Snowgrass Creek Fault constrained by our earthquake locations.

545 Including the Snowgrass Creek Fault as a separation between the western side of  
 546 the Kekerengu Fault and the western (inland) side of the Jordan Thrust reduces the re-  
 547 quired dextral motion from 6.2 m on the Kekerengu to 3.3 m on the Jordan Thrust. The  
 548 difference in these estimated offsets corresponds well with the difference in dextral off-  
 549 sets measured by Kearse et al. (2018), which rise from c. 1–8 m on the Jordan Thrust,  
 550 and are generally between 10–12 m on the Kekerengu Fault (see Supplementary Figures  
 551 S2 and S3). Without the Snowgrass Creek Fault, block offsets require 5.1 m and 5.0 m  
 552 of dextral slip on the Kekerengu and Jordan Thrust Faults, which does not allow for change  
 553 in the change in dextral offset observed. Our estimates do not capture the total slip on  
 554 the faults because we use spatially averaged displacements in off-fault blocks to capture  
 555 the general kinematics. Nevertheless, the change in slip between the Kekerengu and Jor-  
 556 dan Thrust cannot be accommodated without some additional deformation, and the Snow-  
 557 grass Creek Fault provides a viable structure for this deformation.

558 We suggest, therefore, that the Kaikōura earthquake propagated from the Hundalee  
 559 Fault onto the offshore thrust system, which then activated the Papatea and Snowgrass

560 Creek Faults, which in turn triggered slip on the Kekerengu Fault. In this model, the  
 561 role of the Jordan Thrust is minor, and the extension of aftershocks between the Jor-  
 562 dan Thrust to the Whites Fault is a consequence of the underlying thrust system. This  
 563 scenario agrees with the dynamic rupture simulation of Ulrich et al. (2019), but is at odds  
 564 with that of Ando and Kaneko (2018) whose model did not result in significant slip on  
 565 the Papatea Fault. We note that both Ando and Kaneko (2018) and Ulrich et al. (2019)  
 566 have used a shallower dip on the offshore thrust system than the 45–60° dip found here,  
 567 which results in a reduced possible stress-drop in the model of Ando and Kaneko (2018),  
 568 making it a less favourable rupture pathway in their model.

569 The Snowgrass Creek Fault also appears to link with the Clarence Fault, a key com-  
 570 ponent of the Marlborough Fault system (Van Dissen & Nicol, 2009) that did not rup-  
 571 ture in the Kaikōura earthquake. One of the earliest aftershocks we detected, a  $M_L$ 4.8  
 572 within nine minutes of the mainshock origin time, occurred at the junction of the Snow-  
 573 grass Creek and Clarence Faults, suggesting that the Clarence Fault may have been ac-  
 574 tive early in the aftershock sequence. That neither the Hope nor the Clarence Faults had  
 575 significant co-seismic rupture despite evident triggered aftershocks, remains an intrigu-  
 576 ing observation.

### 577 4.3 Subduction Interface

578 We observe no earthquakes consistent with slip on the subduction interface beneath  
 579 the majority of the upper-plate faults (Figure 7). The few earthquakes observed close  
 580 to the subduction interface (e.g. at 23 km depth in Figure 5) show normal-faulting mech-  
 581 anisms, consistent with extension in the down-going plate, and were active prior to the  
 582 Kaikōura earthquake. Some earthquakes consistent with subduction interface slip oc-  
 583 cur beneath the Cape Campbell region, as shown by Lanza et al. (2019) and here (Fig-  
 584 ure 8), but not all show mechanisms consistent with interface slip here. It may be that  
 585 the northern-tip of South Island is the point where the subduction interface becomes seis-  
 586 mically active, as proposed by Henrys et al. (2020).

587 When considering the significance of a lack of aftershocks in our catalog on the sub-  
 588 duction interface it is important to restate the limitations of matched-filter catalogs. Such  
 589 catalogs by definition only contain earthquakes similar to those in the template dataset:  
 590 if we do not have any subduction interface earthquakes in our template set then we should  
 591 not be surprised to see no subduction related events in the final catalog. However, our  
 592 template catalog is composed of all earthquakes in the GeoNet catalog between 13 Novem-  
 593 ber 2016 and 13 May 2017 larger than  $M_L$ 3 (Lanza et al., 2019). As such, any missing  
 594 seismicity should be of small magnitude and therefore likely contributed minimally to  
 595 the total (post-seismic) moment release.

596 Our dataset provides no direct constraints on whether the subduction interface slipped  
 597 co-seismically, but by more accurately mapping crustal seismicity we are able to robustly  
 598 demonstrate the existence of offshore thrust faulting south of the Kekerengu Fault. Such  
 599 offshore faulting has been previously used in models that recreate co-seismic data with-  
 600 out the need for significant slip on a subduction source (e.g. Gusman et al., 2018; Clark  
 601 et al., 2017). Incorporating more realistic models of crustal faulting at depth, derived  
 602 from our catalog, may provide greater constraints on the co-seismic role of the subduc-  
 603 tion interface.

604 The lack of aftershocks on the subduction interface does not preclude afterslip on  
 605 the interface because this afterslip could be aseismic. However, it seems unlikely that  
 606 if the subduction interface is aseismic in the post-seismic period that it would have con-  
 607 tributed significantly to the co-seismic seismic wavefield. The published models of post-  
 608 seismic slip have used simple models of crustal faulting (for instance Wallace et al. (2018)  
 609 use four crustal fault sources attempting to simulate the Humps, Kekerengu/Jordan Thrust,

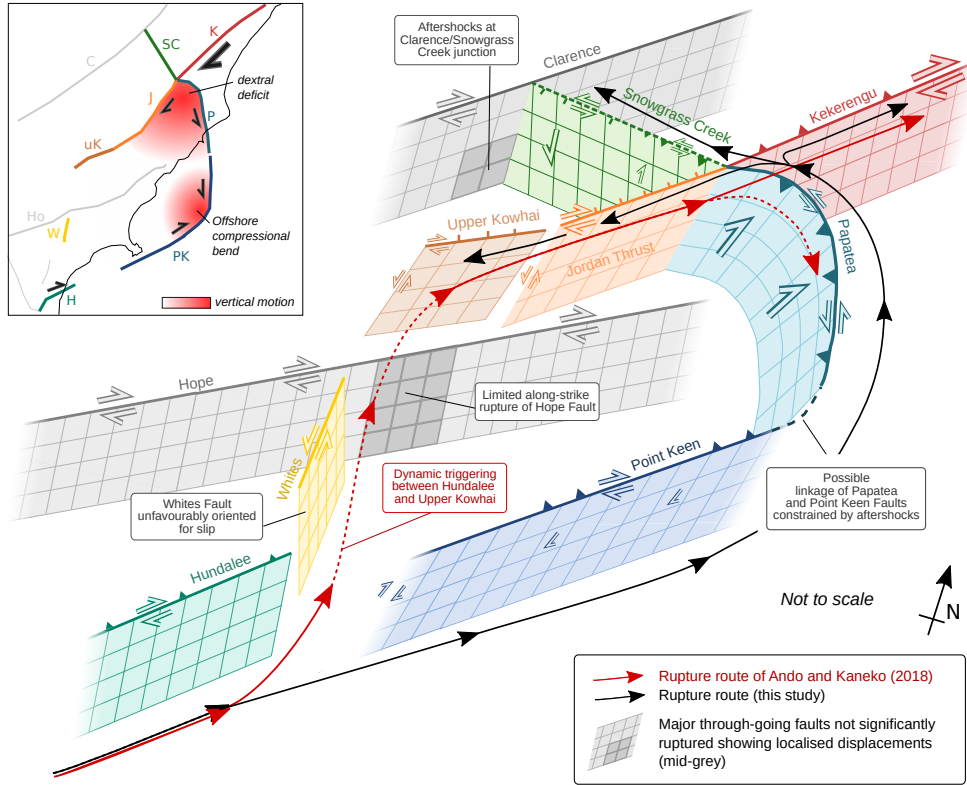


**Figure 6.** Schematic, not-to scale cartoon illustrating links between faults in the stepover region between the southern faults and the high slip Kekerengu Fault, and how the Papatea Fault may operate as a restraining pop-up. Faults in grey represent major through-going structures of the Marlborough Fault Zone (the Hope and Clarence Faults) which did not have significant co-seismic rupture, but which may have localised slip at depth near fault junctions as indicated by darker grey shading. Coloured, outlined arrows on faults show sense of co-seismic motion, approximately scaled by size to show relative slip magnitudes between different faults. The thin red line with arrows shows preferred inland rupture route of Ando and Kaneko (2018) via the Whites Fault (inferred, dashed line) and triggered slip on the Papatea (also denoted by dashed line). The thin black line with arrows shows our preferred offshore rupture route, with bi-lateral rupture originating from the Papatea-Kekerengu-Snowgrass Creek-Jordan Thrust junction. Inset shows simplified map view of faults, coloured as in main plot, illustrating how the Papatea-Point Keen connection forms an offshore compressional bend with anticipated vertical motion.

610 Needles and an offshore thrust fault). The simplicity in crustal faults may lead to inac-  
611 curate mapping of slip onto the underlying subduction interface.

612 For example, in the Cape Campbell area, at the northern tip of South Island, strong  
613 co- and post-seismic uplift occurred (Wallace et al., 2018). This uplift includes a large  
614 short-wavelength component: the uplift at GNSS station CMBL is more than triple that  
615 at station WITH (Figures 1 and 9), within a few tens of kilometres. WITH and CMBL  
616 are separated by the faults that ruptured in the Lake Grassmere earthquake (Hamling  
617 et al., 2014), which were re-invigorated during the Kaikōura aftershock sequence (Fig-  
618 ure 8). These faults are more shallowly dipping than the Needles Fault, and have a sig-  
619 nificant reverse component (Hamling et al., 2014), but the pattern of uplift observed in  
620 the Kaikōura earthquake is the reverse of that in the Lake Grassmere earthquake (Hamling  
621 et al., 2014). This suggests that either the Lake Grassmere and Cook Strait Faults were  
622 reactivated with a normal sense of motion (but we do not observe normal focal mech-  
623 anisms in this region), or other reverse faults dipping to the East, such as the London  
624 Hills Fault, were responsible for this short-wavelength uplift. No faults between WITH  
625 and CMBL with this sense of motion were included in the afterslip model of Wallace et  
626 al. (2018). Inclusion of these faults, which have a strong aftershock signature (Figure 8)  
627 may reduce the need for interface slip beneath Cape Campbell.

628 Incorporating more realistic and complex crustal faulting is unlikely to completely  
629 remove the need for slip on the underlying subduction interface: crustal faults are likely  
630 to help to explain short-wavelength geodetic features, but not the long-wavelength fea-  
631 tures seen in both the post-seismic InSAR and GNSS data (Wallace et al., 2018).

632 Recent modelling work by Eberhart-Phillips et al. (2021), constrained by seismic  
633 attenuation modeling results, shows that deformation between the subducted Pacific plate  
634 and overlying Australian plate is likely to be ductile with no clear interface structure.  
635 In this scenario, ductile deformation rather than interface slip may be controlling the long-  
636 wavelength post-seismic signature. Such ductile deformation would likely be aseismic,  
637 consistent with both the geodetic signature and the lack of aftershocks.

#### 638 4.4 Termination

639 The Kaikōura earthquake terminated near Cape Campbell, at the north-eastern  
640 tip of South Island. Surface ruptures were mapped on the Needles (offshore, but with-  
641 out rupture of the nearby/adjoining Boo Boo Fault (Kearse et al., 2018)), Marfells Beach,  
642 Cape Campbell Road and Lighthouse Faults (Litchfield et al., 2018). The rupture ter-  
643 minated despite the existence of multiple other pre-existing mapped faults in the region.  
644 The Cape Campbell region also hosted the 2013 Cook Strait earthquake sequence, in-  
645 cluding the  $M_W$ 6.6 Cook Strait earthquake on 21 July 2013, and the subsequent  $M_W$ 6.6  
646 Lake Grassmere earthquake on 16 August 2013 (Hamling et al., 2014). This region is also  
647 close to the modelled southern rupture extend of the  $M$ 8 1855 Wairarapa earthquake  
648 (Darby & Beanland, 1992; Rodgers & Little, 2006).

649 Dynamic rupture simulations have been able to simulate arrest on the Needles Fault  
650 (Ulrich et al., 2019; Ando & Kaneko, 2018), either by invoking a small ( $10^\circ$  clockwise)  
651 rotation in the regional stress field (Ando & Kaneko, 2018), or by enforcing reduced pre-  
652 stress on the Needles Fault while rotating the stress field in the opposite direction (Ulrich  
653 et al., 2019). The two shallow ( $<25$  km)  $S_{Hmax}$  estimations from Townend et al. (2012)  
654 in the region (their clusters 16 and 11) suggest a possible clockwise rotation as used by  
655 Ando and Kaneko (2018). The counter-clockwise rotated cluster in Cook Strait (clus-  
656 ter 18) has a centroid at 42 km depth and is likely related to stresses associated with sub-  
657 duction interface beneath. We therefore favour a clockwise rotation to an  $S_{Hmax}$  orien-  
658 tation of c.  $110^\circ$  which reduces the potential stress drop on the Needles Fault and leads  
659 to the spontaneous termination in the model of Ando and Kaneko (2018). This rotation  
660 is also consistent with the earlier work of Balfour et al. (2005).

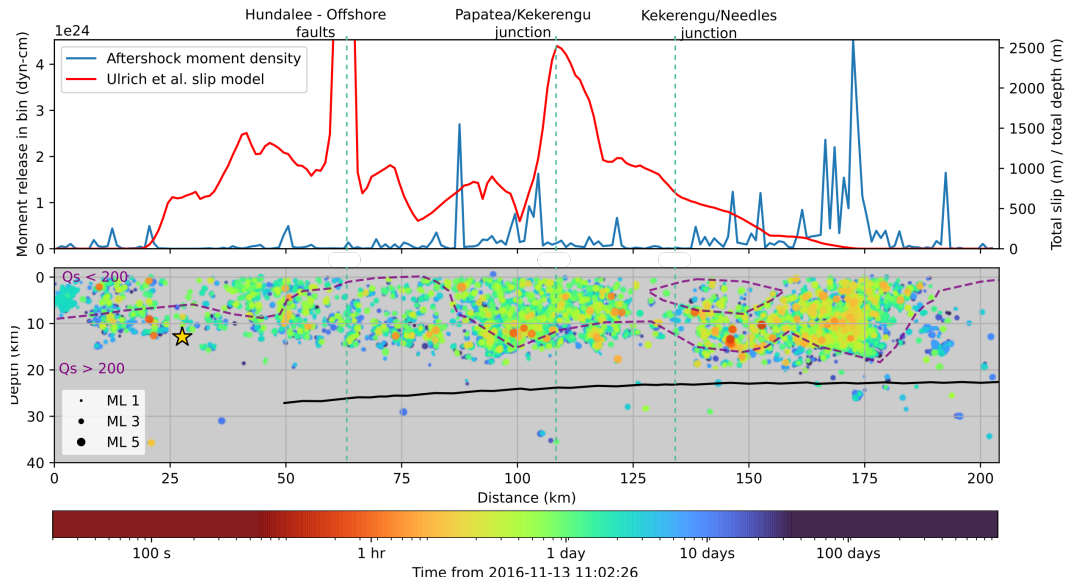


**Figure 7.** Along-strike earthquake distribution, along line A-A' shown on Figure 2. Top: Aftershock moment density (blue) computed in 1 km bins perpendicular to the cross-section, and slip density derived by Ulrich et al. (2019) (red). Note that the projection of all slip in this 3D fault geometry onto a single plane results in the summation of slip across multiple fault strands. The peak in slip around 65 km along the section occurs at the corner between the Stone Jug and Hundalee faults and is likely unrealistic, and in part due to the projection of slip on a single plane. Bottom: Aftershock locations coloured by time since 30 s prior to the the Kaikōura mainshock. Note that the colour-scale is logarithmic. The location of the epicentre of the mainshock is shown by a gold star, and the depth of the interface from C. A. Williams et al. (2013) is shown as a solid line. The purple dashed contour marks the  $Q_s=200$  contour from the NZW3D 2.2 model (Henry et al., 2020).

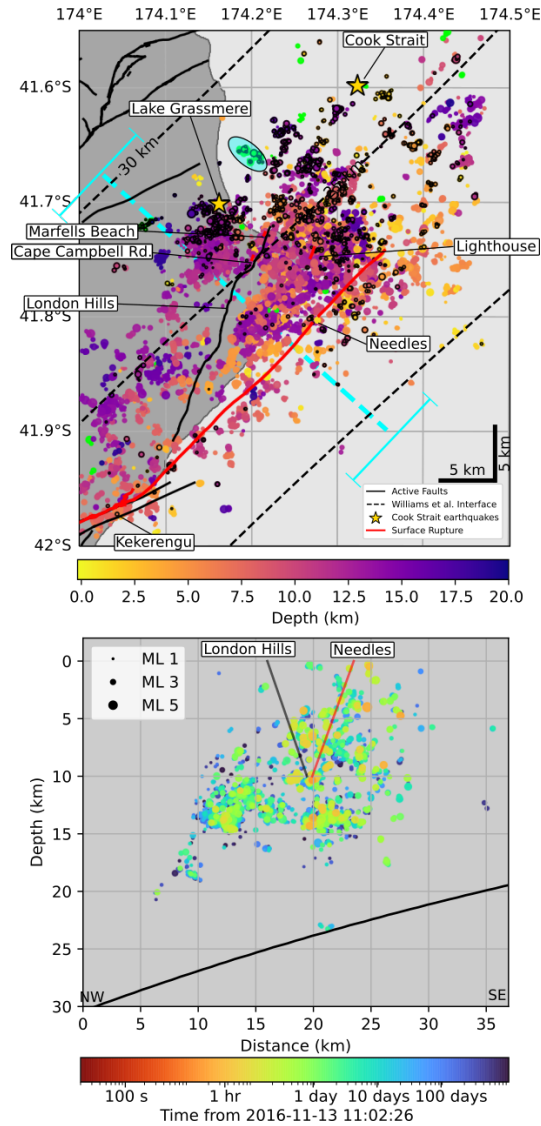


**Figure 8.** Earthquake locations near the termination of the Kaikōura earthquake. Top: Map view of earthquake relocations coloured by depth. Earthquakes deeper than 20 km are coloured green. Earthquakes with black outlines mark events that occurred prior to the Kaikōura mainshock, including events triggered by the Cook Strait and Lake Grassmere earthquakes in 2013, which are plotted as gold stars. Active faults without surface rupture from the Kaikōura earthquake are plotted as black lines, and those with surface rupture are plotted in red. Black dashed contours show the model of the Hikurangi subduction interface from C. A. Williams et al. (2013). The teal oval outlines the events close to the subduction interface that have mechanisms possibly related to slip on the interface as identified by Lanza et al. (2019). The dashed cyan line marks the cross-section plotted below, and the width of the swath (10 km) is shown at each end of the cross-section line. Bottom: Cross-section of earthquake locations coloured by time after 30 s prior to the Kaikōura mainshock within 5 km of the cross-section line. The subduction interface is shown as a curved solid black line, and the projections of the Needles (surface dip of 70°, (Litchfield et al., 2018)) and London Hills (surface dip of 70° (R. Langridge et al., 2016)) faults to 10 km depth are shown.

Neither of the above-mentioned dynamic rupture models (Ando & Kaneko, 2018; Ulrich et al., 2019) includes slip on other faults around Cape Campbell, despite the mapped surface ruptures (Litchfield et al., 2018) and the diffuse aftershocks mapped here and by Lanza et al. (2019). Importantly, the inferred rupture plane of the Cook Strait earthquakes is rotated c. 9° clockwise of the average strike of the Needles Fault (Hamling et al., 2014), resulting in a more favourable orientation for slip on these faults in the regional stress-field. Interestingly we see a general paucity of earthquakes on the Needles Fault (Figure 8) compared to faults directly beneath Cape Campbell despite the co-seismic rupture of the Needles Fault. We suggest that this may be due to the unfavourable orientation of this fault. We also favour a more steeply dipping (near-vertical) Needles Fault, with much of the reverse component of deformation taken up by shallower dipping faults to the West.

Because the templates we use, despite having been constructed exclusively from aftershocks of the Kaikōura earthquake, detect aftershocks of the Cook Strait sequence (but not the mainshocks), the Kaikōura aftershock sequence must include re-rupture of favourably oriented faults that were active during the Cook Strait aftershock sequence. Focal mechanisms of aftershocks in this region include multiple dextral-reverse mechanisms striking c. 055°, similar to the Cook Strait mainshocks.

We consider two possibilities for the cause of the activation of the Cook Strait sequence fault(s) by the Kaikōura earthquake: (1) the Kaikōura earthquake co-seismically ruptured the more favourably oriented “Cook Strait Fault”; (2) seismicity on the “Cook Strait Fault” was triggered post-seismically. As computed by Ulrich et al. (2019), the maximum Coulomb failure stress ( $\Delta$ CFS) reduction on the Needles Fault due to the Cook Strait sequence is small (c. 0.1 MPa), and is strongly heterogeneous. However, the stress drops on the “Cook Strait Fault” itself due to the Cook Strait and Lake Grassmere earthquakes are 1 MPa and 3.5 MPa respectively. We hypothesise that this resulted in reduced pre-stress on the “Cook Strait Fault”, ensuring that the Kaikōura earthquake could not generate significant rupture through this more favourably oriented fault, either co-seismically or post-seismically. Changes in frictional properties on the “Cook Strait Fault” may also act to inhibit rupture, but we have no direct observations of the frictional properties, nor how they vary in time for these faults.

Our aftershock locations do not show clear evidence for a structural boundary within Cook Strait as the control for rupture termination. Instead we observe a consistent migration of aftershocks away from the inferred rupture termination point into Cook Strait (see section 4.5, Figure 7 and Supplementary Figure S9). Nevertheless, the aftershocks do concentrate within the region of low  $Q$  (high seismic attenuation), as demonstrated by Henrys et al. (2020). (Henrys et al., 2020) suggested that the change in seismic properties in Cook Strait may be linked to changes in interface coupling, upper-plate deformation and strain-accumulation, which may play a role in rupture termination. In general the aftershocks are found to have occurred within regions of low  $Q$ , which may be indicative of regions of higher fracturing or damage, more capable of hosting seismicity (Henrys et al., 2020).

We suggest that a combination of an unfavourably oriented Needles Fault, reduced pre-stress due to prior rupture of other nearby faults, and the presence of diffuse faulting around Cape Campbell, served to terminate the rupture near Cape Campbell.

#### 4.5 Post-seismic

The catalog we present here is dominated by aftershocks providing important information on deformation processes following complex co-seismic slip. Spatially, several key features are apparent in the post-seismic period (Figure 7). Firstly, the peak aftershock densities occur at the rupture termination point near Cape Campbell, and in the step-over region between the southern and northern rupture domains. Strong aftershock

712 activity near rupture terminations where there are elevated stress concentrations is com-  
 713 mon (King et al., 1994), and we do see many aftershocks surrounding the Needles Fault  
 714 (Figure 8): however, the majority of aftershocks around Cape Campbell occur in a dis-  
 715 tributed region between the Needles Fault and the location of the 2013 Cook Strait se-  
 716 quence. The patch of aftershocks around Cape Campbell expands in time, following a  
 717 roughly log-time expansion, and seems to expand bilaterally (Figure 7, Supplementary  
 718 Figure S9).

719 As previously reported, there are very few aftershocks associated with the Papatea  
 720 Fault and the highest-slip patch of the Kekerengu Fault, which we interpret to be seg-  
 721 ments that experienced near-total stress-drop. The high-slip patch of the Kekerengu Fault  
 722 separates the two regions of high aftershock density and may provide a limiting control  
 723 to the aftershock sequence.

724 In the south, we see a continuation of aftershocks beyond the southern rupture ter-  
 725 mination point, and clustered triggered off-fault seismicity. We also note that, although  
 726 there are aftershocks on the Leader and surrounding faults, we also see a continuous trend  
 727 of aftershocks joining the Humps and Hundalee Faults, effectively cutting off this block,  
 728 and potentially accommodating block rotation as proposed by T. Wang et al. (2020).

729 Comparison of GNSS displacements with earthquake rates in regions surrounding  
 730 the GNSS site shows that aftershock rates are generally proportional to displacement  
 731 rates (Figure 9). The catalog presented here is sufficiently detailed to map earthquakes  
 732 to individual faults, but the published post-seismic slip models do not have sufficiently  
 733 detailed crustal fault resolution to directly compare aftershocks with afterslip. Because  
 734 of the complexity of the earthquake, GNSS displacement measured at a single site is likely  
 735 to correspond to slip on multiple fault sources, rendering direct comparison of geodetic  
 736 data with seismicity non-unique. Nevertheless, despite the range of faulting and co-seismic  
 737 slip, it appears that aftershock distributions correlate well with geodetically determined  
 738 displacements, suggesting that aftershocks are driven by local afterslip (Frank et al., 2017;  
 739 Perfettini et al., 2018).

## 740 5 Conclusions

741 The 2016 M 7.8 Kaikōura earthquake is widely regarded as one of the most com-  
 742 plex earthquakes in recorded history (Hamling, 2020). Detailed mapping of seismicity  
 743 around the faults that ruptured in the Kaikōura earthquake further emphasises this com-  
 744 plexity: at-least in the post-seismic period, multiple faults that did not have surface rup-  
 745 ture are activated including two of the high slip-rate and high hazard Marlborough Faults  
 746 (the Clarence and the Hope Faults). However, the additional faults observable through  
 747 this mapping may also simplify some of the kinematics of the rupture by providing ad-  
 748 ditional structures to host variations in slip between nearby fault segments.

749 To address the original outstanding questions outlined in Section 1.3, and as dis-  
 750 cussed in Sections 4.1–4.5, our conclusions are as follows:

- 751 1a. The mainshock unequivocally nucleated on the Humps Fault. Previous scatter in  
 752 published locations can be attributed to inappropriate location methods or data  
 753 quality issues which we have thoroughly addressed in this study.
- 754 1b. We do not observe any precursory activity in our catalog, but this is likely a lim-  
 755 itation of using the aftershock-derived template set. We do observe one foreshock  
 756 7 s prior to the mainshock, however the sparsity of seismic stations limits our abil-  
 757 ity to investigate further.
- 758 2a. Offshore thrust faulting illuminated by aftershocks suggests a physical connection  
 759 between the Hundalee and Papatea Faults, which may explain anomalously high  
 760 slip on the Papatea Fault and provides a likely southern/offshore rupture route.

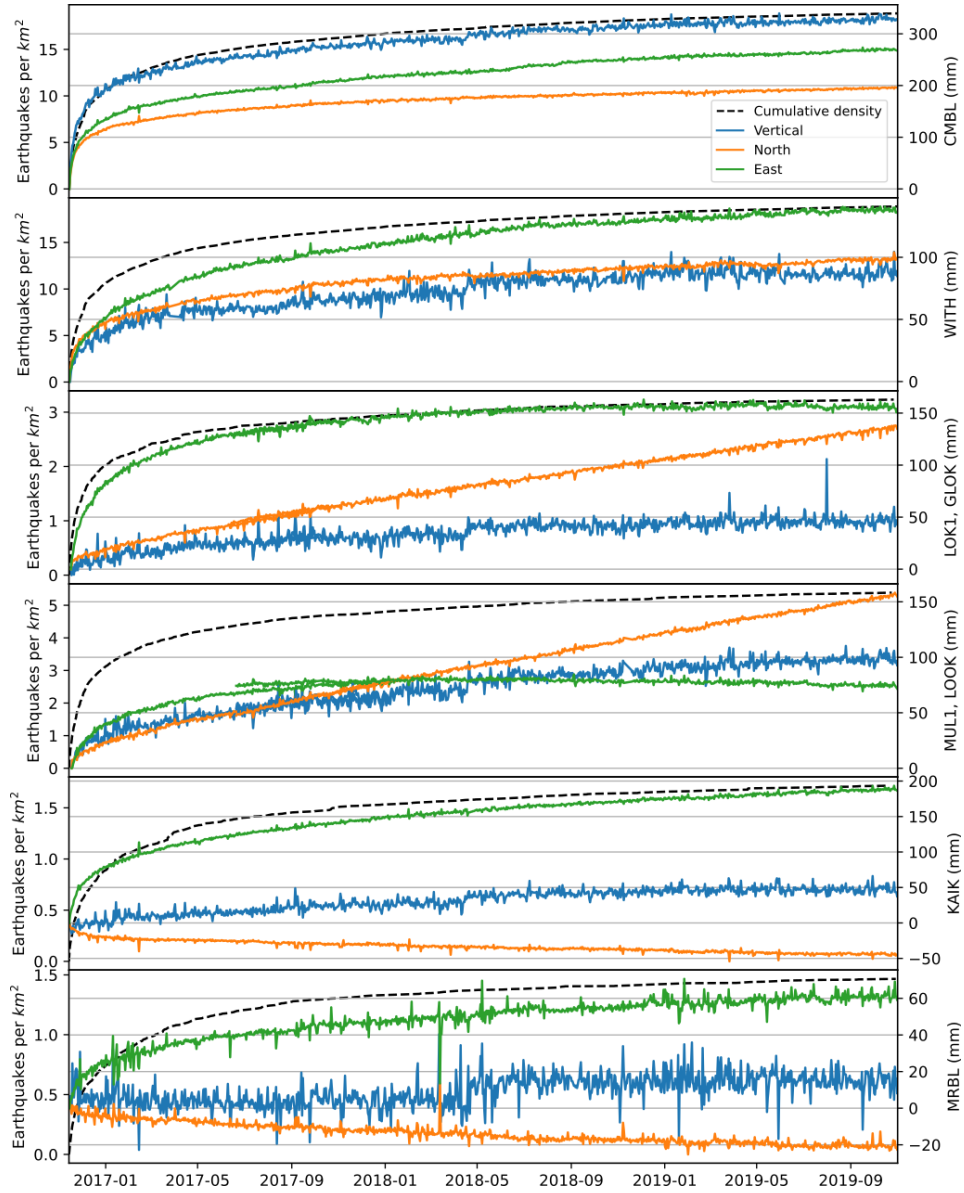


**Figure 9.** GPS time-series and cumulative aftershock density for regions around the Kaikōura afterslip region. Regions are ordered north (top) to south. GPS displacements for sites CMBL, WITH, KAIK and MRBL have a long-term gradient removed (calculated between 2015/01/01 to 2016/11/1). Sites LOK1, GLOK, MUL1 and LOOK have not had any gradient removed because they were not active prior to Kaikōura. Data from stations GLOK and LOOK have been shifted to have matching displacements at the end of the recording periods of LOK1 and MUL1 respectively. Note that the overlap is imperfect, but provides a representative view of displacement in the region. In general the evolution of the aftershock sequence matches the evolution of the displacement for these regions, however there are strong differences across the regions highlighting different amounts of afterslip.

- 761 2b. The Snowgrass Creek-Papatea-Jordan Thrust-Kekerengu system acts as a quadru-  
 762 ple junction providing a means of distributing the drop in slip between the Kek-  
 763 erengu and Jordan Thrust Faults.
- 764 2c. Both the Hope and Clarence Faults were active post-seismically and produced af-  
 765 tershocks, though these were not laterally extensive, and occur near fault junc-  
 766 tions or transitional zones.
- 767 3. We observe very few aftershocks on the subduction interface. A proportion of the  
 768 afterslip previously mapped onto the subduction interface may instead be accom-  
 769 modated by unmodelled upper crustal faults, such as the previously unidentified  
 770 Snowgrass Creek Fault, the Clarence Fault and diffuse faulting characterised by  
 771 abundant aftershocks near Cape Campbell. However crustal faults are unlikely to  
 772 remove the need for deep deformation to explain the long-wavelength signature  
 773 in the geodetic data, but this deformation likely occurs aseismically.
- 774 4. The rupture terminated near the epicentres of the Lake Grassmere and Cook Strait  
 775 2013 earthquakes, and likely re-ruptured these faults. The Cook Strait and Lake  
 776 Grassmere faults are more favourably oriented for slip than the co-seismically rup-  
 777 tured Needles Fault, and we propose that the combination of unfavourable orien-  
 778 tation of the Needles together with reduced pre-stress on the Lake Grassmere and  
 779 Cook Strait faults was sufficient to cause the rupture to terminate here.
- 780 5. Aftershock concentrate at step-overs in faulting, and at the rupture termination  
 781 near Cape Campbell. The patch of high co-seismic slip on the Kekerengu Fault  
 782 has few aftershocks and potentially experienced near total stress drop, and may  
 783 separate patches of afterslip reducing aftershock productivity.

784 Considering all of the above, we infer that the Kaikōura earthquake nucleated with-  
 785 out significant detectable precursory seismicity on the Humps Fault before transition-  
 786 ing through the Leader/Stone Jug system and onto the Hundalee Fault. The rupture then  
 787 continued directly onto the offshore fault system characterised by reverse slip, elsewhere  
 788 called the Point Keen Fault. Slip then transitioned onto the Papatea Fault, likely by di-  
 789 rectly linked faults at depth in a thrust block bounded by sinistral faulting on the Pa-  
 790 patea and Snowgrass Creek Faults (Figure 6). Within this block, the Jordan Thrust Fault  
 791 was reactivated in an extensional stress regime giving rise to normal motion (in contrast  
 792 to the long-term motion on this fault), and the difference in slip between the Jordan Thrust  
 793 and Kekerengu Faults is accommodated by buried slip on the previously unknown Snow-  
 794 grass Creek Fault.

795 Slip then transitioned onto the Kekerengu Fault, which experienced near-total stress-  
 796 drop in the high slip patch identified by other authors (e.g. Kearse et al., 2018), and char-  
 797 acterised here by a lack of aftershocks. The rupture then propagated onto the Needles  
 798 Fault and other faults around Cape Campbell that were previously ruptured in the 2013  
 799 Cook Strait earthquakes. A combination of an unfavourable stress orientation on the Need-  
 800 les Fault and reduced pre-stress due to recent slip on the Cook Strait and Lake Grass-  
 801 mere faults resulted in the termination of the Kaikōura earthquake at Cape Campbell.  
 802 We see no evidence for seismic slip on an underlying subduction interface, apart from  
 803 a small cluster of interface related seismicity near Cape Campbell. We therefore suggest  
 804 that the boundary between the overriding Australian plate and subduction Pacific plate  
 805 may be ductile beneath much of the Kaikōura earthquake fault system as suggested by  
 806 Eberhart-Phillips et al. (2021).

## 807 Data Availability

808 All waveform data for GeoNet stations were downloaded from GeoNet via their FDSN  
 809 client (last accessed 20 April 2021). All data from the STREWN network (code Z1) were  
 810 downloaded from the IRIS FDSN Client (last accessed 6 June 2021). The catalog gen-  
 811 erated here is available at <https://doi.org/10.5281/zenodo.4717333> (last accessed 24 April

2021) in QUAKEML and CSV format. All code used to generate this catalogue is open-source, and the scripts to complete the workflow are available on github at <https://github.com/calum-chamberlain/kaikoura-aftershocks> (last accessed 28 June 2021).

## Acknowledgments

Chamberlain and Townend are grateful to New Zealand’s Earthquake Commission (EQC) for funding through the EQC Programme in Seismology and Tectonic Geodesy at Victoria University of Wellington, and an EQC Biennial Grant (18/753), and to the Royal Society of New Zealand for funding through the Marsden Fast-Start project 17-VUW-121. Frank, Townend and Chamberlain also received funding for this collaboration through the New Zealand Royal Societies Catalyst Grant scheme. Chamberlain and Warren-Smith are grateful to the New Zealand Ministry of Business, Innovation and Employment for funding through the Endeavour programme: ‘Rapid Characterisation of Earthquakes and Tsunamis (RCET)’. Warren-Smith was funded through GNS Science Ministry of Business Innovation and Employment strategic science investment funding (GNS-SSIF). Initial compute time was provided by the New Zealand eScience Infrastructure (NeSI) for which we are grateful. Later computations were run on Amazon Web Services, with data handling assistance from GeoNet. We acknowledge the New Zealand GeoNet project and its sponsors EQC, GNS Science, LINZ, NEMA and MBIE for providing data used in this study. ObsPy (Krischer et al., 2015) was used extensively throughout this work, figures were made using matplotlib (Hunter, 2007) and cartopy (Met Office, 2010 - 2015), and we are very grateful to the developers and maintainers of these open-source projects who enable complex science. Finally we are grateful to Tim Little, Andy Howell, Carolyn Boulton, James Crampton, Rob Langridge, Laura Wallace, Ian Hamling and others in the New Zealand geoscience community for informative discussions during the preparation of this work.

## References

- Ando, R., & Kaneko, Y. (2018). Dynamic Rupture Simulation Reproduces Spontaneous Multifault Rupture and Arrest During the 2016 Mw 7.9 Kaikoura Earthquake. *Geophysical Research Letters*, *45*(23), 12,875–12,883. Retrieved from <https://agupubs.onlinelibrary.wiley.com/doi/abs/10.1029/2018GL080550> doi: 10.1029/2018GL080550
- Bai, Y., Lay, T., Cheung, K. F., & Ye, L. (2017). Two regions of seafloor deformation generated the tsunami for the 13 November 2016, Kaikoura, New Zealand earthquake. *Geophysical Research Letters*, *44*(13), 6597–6606. Retrieved from <https://agupubs.onlinelibrary.wiley.com/doi/abs/10.1002/2017GL073717> doi: 10.1002/2017GL073717
- Balfour, N., Savage, M., & Townend, J. (2005). Stress and crustal anisotropy in Marlborough, New Zealand: evidence for low fault strength and structure-controlled anisotropy. *Geophysical Journal International*, *163*(3), 1073–1086.
- Beaucé, E., Frank, W. B., & Romanenko, A. (2018). Fast matched filter (FMF): An efficient seismic matched-filter search for both CPU and GPU architectures. *Seismological Research Letters*, *89*(1), 165–172.
- Bradley, B. A., Razafindrakoto, H. N., & Polak, V. (2017). Ground-motion observations from the 14 November 2016 Mw 7.8 Kaikoura, New Zealand, earthquake and insights from broadband simulations. *Seismological Research Letters*, *88*(3), 740–756.
- Bratt, S., & Nagy, W. (1991). The LocSAT Program. *Science Applications International Corporation, San Diego*.
- Cesca, S., Zhang, Y., Mouslopoulou, V., Wang, R., Saul, J., Savage, M., . . . Dahm, T. (2017). Complex rupture process of the Mw 7.8, 2016, Kaikoura earthquake, New Zealand, and its aftershock sequence. *Earth and Planetary Science*

- 863 *Letters*, 478, 110 - 120. Retrieved from <http://www.sciencedirect.com/science/article/pii/S0012821X17304715> doi: <https://doi.org/10.1016/j.epsl.2017.08.024>
- 864  
865
- 866 Chamberlain, C. J., Hopp, C. J., Boese, C. M., Warren-Smith, E., Chambers, D.,  
867 Chu, S. X., ... Townend, J. (2018). EQcorrscan: Repeating and near-  
868 repeating earthquake detection and analysis in python. *Seismological Research*  
869 *Letters*, 89(1), 173–181.
- 870 Chamberlain, C. J., Townend, J., & Gerstenberger, M. C. (2020). RT-EQcorrscan:  
871 Near-Real-Time Matched-Filtering for Rapid Development of Dense Earth-  
872 quake Catalogs. *Seismological Society of America*, 91(6), 3574–3584.
- 873 Christophersen, A., Rhoades, D., Gerstenberger, M., Bannister, S., Becker, J., Pot-  
874 ter, S., & McBride, S. (2017). Progress and challenges in operational earth-  
875 quake forecasting in New Zealand. In *New zealand society for earthquake*  
876 *engineering annual technical conference*.
- 877 Clark, K., Nissen, E., Howarth, J., Hamling, I., Mountjoy, J., Ries, W., ... Strong,  
878 D. (2017). Highly variable coastal deformation in the 2016 MW7.8 Kaikōura  
879 earthquake reflects rupture complexity along a transpressional plate bound-  
880 ary. *Earth and Planetary Science Letters*, 474, 334 - 344. Retrieved from  
881 <http://www.sciencedirect.com/science/article/pii/S0012821X17303722>  
882 doi: <https://doi.org/10.1016/j.epsl.2017.06.048>
- 883 Darby, D. J., & Beanland, S. (1992). Possible source models for the 1855 Wairarapa  
884 earthquake, New Zealand. *Journal of Geophysical Research: Solid Earth*,  
885 97(B9), 12375–12389.
- 886 Diederichs, A., Nissen, E., Lajoie, L., Langridge, R., Malireddi, S., Clark, K., ...  
887 Tagliasacchi, A. (2019). Unusual kinematics of the Papatea fault (2016  
888 Kaikōura earthquake) suggest anelastic rupture. *Science advances*, 5(10),  
889 eaax5703.
- 890 Eberhart-Phillips, D., & Bannister, S. (2015). 3-D imaging of the northern Hiku-  
891 rangi subduction zone, New Zealand: variations in subducted sediment, slab  
892 fluids and slow slip. *Geophysical Journal International*, 201(2), 838–855.
- 893 Eberhart-Phillips, D., Bannister, S., & Reyners, M. (2017, November). *New*  
894 *Zealand Wide model 2.1 seismic velocity model for New Zealand*. Zen-  
895 odo. Retrieved from <https://doi.org/10.5281/zenodo.1043558> doi:  
896 10.5281/zenodo.1043558
- 897 Eberhart-Phillips, D., Ellis, S., Lanza, F., & Bannister, S. (2021). Heterogeneous  
898 material properties – as inferred from seismic attenuation - influenced multi-  
899 ple fault rupture and ductile creep of the Kaikoura Mw 7.8 earthquake, New  
900 Zealand. *Geophysical Journal International*.
- 901 Frank, W. B., Poli, P., & Perfettini, H. (2017). Mapping the rheology of the Central  
902 Chile subduction zone with aftershocks. *Geophysical Research Letters*, 44(11),  
903 5374–5382.
- 904 Frigo, M., & Johnson, S. G. (1998). FFTW: An adaptive software architecture for  
905 the FFT. In *Proceedings of the 1998 ieee international conference on acous-*  
906 *tics, speech and signal processing, icassp'98 (cat. no. 98ch36181)* (Vol. 3, pp.  
907 1381–1384).
- 908 Gusman, A. R., Satake, K., Gunawan, E., Hamling, I., & Power, W. (2018). Con-  
909 tribution from multiple fault ruptures to tsunami generation during the 2016  
910 Kaikoura earthquake. *Pure and Applied Geophysics*, 175(8), 2557–2574.
- 911 Hainzl, S. (2016). Rate-dependent incompleteness of earthquake catalogs. *Seismolog-*  
912 *ical Research Letters*, 87(2A), 337–344.
- 913 Hamling, I. J. (2020). A review of the 2016 Kaikōura earthquake: insights from  
914 the first 3 years. *Journal of the Royal Society of New Zealand*, 50(2), 226-244.  
915 Retrieved from <https://doi.org/10.1080/03036758.2019.1701048> doi: 10  
916 .1080/03036758.2019.1701048
- 917 Hamling, I. J., D’Anastasio, E., Wallace, L. M., Ellis, S., Motagh, M., Samsonov, S.,

- 918 ... Hreinsdóttir, S. (2014). Crustal deformation and stress transfer during  
 919 a propagating earthquake sequence: The 2013 Cook Strait sequence, central  
 920 New Zealand. *Journal of Geophysical Research: Solid Earth*, *119*(7), 6080-  
 921 6092. Retrieved from [https://agupubs.onlinelibrary.wiley.com/doi/abs/](https://agupubs.onlinelibrary.wiley.com/doi/abs/10.1002/2014JB011084)  
 922 [10.1002/2014JB011084](https://agupubs.onlinelibrary.wiley.com/doi/abs/10.1002/2014JB011084) doi: 10.1002/2014JB011084
- 923 Hamling, I. J., Hreinsdóttir, S., Clark, K., Elliott, J., Liang, C., Fielding, E., ...  
 924 Stirling, M. (2017). Complex multifault rupture during the 2016 Mw 7.8  
 925 Kaikoura earthquake, New Zealand. *Science*, *356*(6334). Retrieved from  
 926 <https://science.sciencemag.org/content/356/6334/eaam7194> doi:  
 927 10.1126/science.aam7194
- 928 Harris, R. A., Archuleta, R. J., & Day, S. M. (1991). Fault steps and the dynamic  
 929 rupture process: 2-D numerical simulations of a spontaneously propagating  
 930 shear fracture. *Geophysical Research Letters*, *18*(5), 893–896.
- 931 Henrys, S., Eberhart-Phillips, D., Bassett, D., Sutherland, R., Okaya, D., Sav-  
 932 age, M., ... others (2020). Upper Plate Heterogeneity Along the South-  
 933 ern Hikurangi Margin, New Zealand. *Geophysical Research Letters*, *47*(4),  
 934 e2019GL085511.
- 935 Holden, C., Kaneko, Y., D’Anastasio, E., Benites, R., Fry, B., & Hamling, I. J.  
 936 (2017). The 2016 Kaikōura Earthquake Revealed by Kinematic Source In-  
 937 version and Seismic Wavefield Simulations: Slow Rupture Propagation on a  
 938 Geometrically Complex Crustal Fault Network. *Geophysical Research Letters*,  
 939 *44*(22), 11,320–11,328. Retrieved from [https://agupubs.onlinelibrary](https://agupubs.onlinelibrary.wiley.com/doi/abs/10.1002/2017GL075301)  
 940 [.wiley.com/doi/abs/10.1002/2017GL075301](https://agupubs.onlinelibrary.wiley.com/doi/abs/10.1002/2017GL075301) doi: 10.1002/2017GL075301
- 941 Howell, A., Nissen, E., Stahl, T., Clark, K., Kearse, J., Van Dissen, R., ... Jones,  
 942 K. (2020). Three-Dimensional Surface Displacements During the 2016 MW  
 943 7.8 Kaikōura Earthquake (New Zealand) From Photogrammetry-Derived Point  
 944 Clouds. *Journal of Geophysical Research: Solid Earth*, *125*(1), e2019JB018739.  
 945 Retrieved from [https://agupubs.onlinelibrary.wiley.com/doi/abs/](https://agupubs.onlinelibrary.wiley.com/doi/abs/10.1029/2019JB018739)  
 946 [10.1029/2019JB018739](https://agupubs.onlinelibrary.wiley.com/doi/abs/10.1029/2019JB018739) (e2019JB018739 2019JB018739) doi: 10.1029/  
 947 2019JB018739
- 948 Hunter, J. D. (2007). Matplotlib: A 2D graphics environment. *Computing in Science*  
 949 *& Engineering*, *9*(3), 90–95. doi: 10.1109/MCSE.2007.55
- 950 Illsley-Kemp, F., Barker, S. J., Wilson, C. J., Chamberlain, C. J., Hreinsdóttir, S.,  
 951 Ellis, S., ... Wadsworth, F. B. (2021). Volcanic unrest at Taupō volcano  
 952 in 2019: Causes, mechanisms and implications. *Geochemistry, Geophysics,*  
 953 *Geosystems*, e2021GC009803. doi: 10.1029/2021GC009803
- 954 Kaiser, A., Balfour, N., Fry, B., Holden, C., Litchfield, N., Gerstenberger, M., ...  
 955 Gledhill, K. (2017, 04). The 2016 Kaikōura, New Zealand, Earthquake:  
 956 Preliminary Seismological Report. *Seismological Research Letters*, *88*(3),  
 957 727–739. Retrieved from <https://doi.org/10.1785/0220170018> doi:  
 958 10.1785/0220170018
- 959 Kearse, J., Little, T. A., Van Dissen, R. J., Barnes, P. M., Langridge, R., Moun-  
 960 tjoy, J., ... Hemphill-Haley, M. (2018, 04). Onshore to Offshore Ground-  
 961 Surface and Seabed Rupture of the Jordan–Kekerengu–Needles Fault Network  
 962 during the 2016 Mw 7.8 Kaikōura Earthquake, New Zealand. *Bulletin of*  
 963 *the Seismological Society of America*, *108*(3B), 1573–1595. Retrieved from  
 964 <https://doi.org/10.1785/0120170304> doi: 10.1785/0120170304
- 965 Kennett, B., & Engdahl, E. (1991). Traveltimes for global earthquake location and  
 966 phase identification. *Geophysical Journal International*, *105*(2), 429–465.
- 967 King, G. C., Stein, R. S., & Lin, J. (1994). Static stress changes and the triggering  
 968 of earthquakes. *Bulletin of the Seismological Society of America*, *84*(3), 935–  
 969 953.
- 970 Klinger, Y., Okubo, K., Vallage, A., Champenois, J., Delorme, A., Rougier, E., ...  
 971 others (2018). Earthquake damage patterns resolve complex rupture processes.  
 972 *Geophysical Research Letters*, *45*(19), 10–279.

- 973 Krischer, L., Megies, T., Barsch, R., Beyreuther, M., Lecocq, T., Caudron, C., &  
 974 Wassermann, J. (2015). ObsPy: A bridge for seismology into the scientific  
 975 Python ecosystem. *Computational Science & Discovery*, 8(1), 014003.
- 976 Lamb, S., Arnold, R., & Moore, J. D. (2018). Locking on a megathrust as a cause  
 977 of distributed faulting and fault-jumping earthquakes. *Nature Geoscience*,  
 978 11(11), 871–875.
- 979 Langridge, R., Ries, W., Litchfield, N., Villamor, P., Van Dissen, R., Barrell, D., ...  
 980 others (2016). The New Zealand active faults database. *New Zealand Journal*  
 981 *of Geology and Geophysics*, 59(1), 86–96.
- 982 Langridge, R. M., Rowland, J., Villamor, P., Mountjoy, J., Townsend, D. B., Nis-  
 983 sen, E., ... Hamling, I. (2018, 06). Coseismic Rupture and Preliminary Slip  
 984 Estimates for the Papatea Fault and Its Role in the 2016 Mw 7.8 Kaikōura,  
 985 New Zealand, Earthquake. *Bulletin of the Seismological Society of America*,  
 986 108(3B), 1596-1622. Retrieved from <https://doi.org/10.1785/0120170336>  
 987 doi: 10.1785/0120170336
- 988 Lanza, F., Chamberlain, C. J., Jacobs, K., Warren-Smith, E., Godfrey, H. J., Ko-  
 989 rtink, M., ... Eberhart-Phillips, D. (2019). Crustal Fault Connectivity of the  
 990 Mw 7.8 2016 Kaikōura Earthquake Constrained by Aftershock Relocations.  
 991 *Geophysical Research Letters*, 46(12), 6487-6496. Retrieved from [https://](https://agupubs.onlinelibrary.wiley.com/doi/abs/10.1029/2019GL082780)  
 992 [agupubs.onlinelibrary.wiley.com/doi/abs/10.1029/2019GL082780](https://agupubs.onlinelibrary.wiley.com/doi/abs/10.1029/2019GL082780) doi:  
 993 10.1029/2019GL082780
- 994 Lienert, B. R., & Havskov, J. (1995). A computer program for locating earthquakes  
 995 both locally and globally. *Seismological Research Letters*, 66(5), 26–36.
- 996 Litchfield, N. J., Villamor, P., Dissen, R. J. V., Nicol, A., Barnes, P. M., A. Barrell,  
 997 D. J., ... others (2018). Surface rupture of multiple crustal faults in the 2016  
 998 M w 7.8 Kaikōura, New Zealand, Earthquake. *Bulletin of the Seismological*  
 999 *Society of America*, 108(3B), 1496–1520.
- 1000 Liu, C., Lay, T., Brodsky, E. E., Dascher-Cousineau, K., & Xiong, X. (2019). Co-  
 1001 seismic Rupture Process of the Large 2019 Ridgecrest Earthquakes From  
 1002 Joint Inversion of Geodetic and Seismological Observations. *Geophys-*  
 1003 *ical Research Letters*, 46(21), 11820-11829. Retrieved from [https://](https://agupubs.onlinelibrary.wiley.com/doi/abs/10.1029/2019GL084949)  
 1004 [agupubs.onlinelibrary.wiley.com/doi/abs/10.1029/2019GL084949](https://agupubs.onlinelibrary.wiley.com/doi/abs/10.1029/2019GL084949) doi:  
 1005 <https://doi.org/10.1029/2019GL084949>
- 1006 Lomax, A., Virieux, J., Volant, P., & Berge-Thierry, C. (2000). Probabilistic earth-  
 1007 quake location in 3D and layered models. In *Advances in seismic event location*  
 1008 (pp. 101–134). Springer.
- 1009 Met Office. (2010 - 2015). Cartopy: a cartographic python library with a Mat-  
 1010 plotlib interface [Computer software manual]. Exeter, Devon. Retrieved from  
 1011 <https://scitools.org.uk/cartopy>
- 1012 Michailos, K., Smith, E. G., Chamberlain, C. J., Savage, M. K., & Townend, J.  
 1013 (2019). Variations in seismogenic thickness along the Central Alpine Fault,  
 1014 New Zealand, revealed by a decade’s relocated microseismicity. *Geochemistry,*  
 1015 *Geophysics, Geosystems*, 20(1), 470–486.
- 1016 Mouslopoulou, V., Saltogianni, V., Nicol, A., Oncken, O., Begg, J., Babeyko, A.,  
 1017 ... Moreno, M. (2019). Breaking a subduction-termination from top  
 1018 to bottom: The large 2016 Kaikōura Earthquake, New Zealand. *Earth*  
 1019 *and Planetary Science Letters*, 506, 221 - 230. Retrieved from [http://](http://www.sciencedirect.com/science/article/pii/S0012821X18306162)  
 1020 [www.sciencedirect.com/science/article/pii/S0012821X18306162](http://www.sciencedirect.com/science/article/pii/S0012821X18306162) doi:  
 1021 <https://doi.org/10.1016/j.epsl.2018.10.020>
- 1022 Nicol, A., Khajavi, N., Pettinga, J. R., Fenton, C., Stahl, T., Bannister, S., ... Mc-  
 1023 Coll, S. T. (2018, 05). Preliminary Geometry, Displacement, and Kinematics  
 1024 of Fault Ruptures in the Epicentral Region of the 2016 Mw 7.8 Kaikōura,  
 1025 New Zealand, Earthquake. *Bulletin of the Seismological Society of America*,  
 1026 108(3B), 1521-1539. Retrieved from <https://doi.org/10.1785/0120170329>  
 1027 doi: 10.1785/0120170329

- 1028 Okada, T., Iio, Y., Matsumoto, S., Bannister, S., Ohmi, S., Horiuchi, S., ... others  
 1029 (2019). Comparative tomography of reverse-slip and strike-slip seismotectonic  
 1030 provinces in the northern South Island, New Zealand. *Tectonophysics*, 765,  
 1031 172–186.
- 1032 Peng, Z., Fry, B., Chao, K., Yao, D., Meng, X., & Jolly, A. (2018, 05). Remote Trig-  
 1033 gering of Microearthquakes and Tremor in New Zealand following the 2016 Mw  
 1034 7.8 Kaikōura Earthquake. *Bulletin of the Seismological Society of America*,  
 1035 108(3B), 1784–1793. Retrieved from <https://doi.org/10.1785/0120170327>  
 1036 doi: 10.1785/0120170327
- 1037 Perfettini, H., Frank, W., Marsan, D., & Bouchon, M. (2018). A model of aftershock  
 1038 migration driven by afterslip. *Geophysical Research Letters*, 45(5), 2283–2293.
- 1039 Plesch, A., Shaw, J. H., Ross, Z. E., & Hauksson, E. (2020). Detailed 3D Fault Rep-  
 1040 resentations for the 2019 Ridgecrest, California, Earthquake Sequence. *Bulletin*  
 1041 *of the Seismological Society of America*, 110(4), 1818–1831.
- 1042 Rattenbury, M., & Isaac, M. (2012). The QMAP 1: 250 000 geological map of New  
 1043 Zealand project. *New Zealand Journal of Geology and Geophysics*, 55(4), 393–  
 1044 405.
- 1045 Ristau, J. (2013). Update of regional moment tensor analysis for earthquakes in New  
 1046 Zealand and adjacent offshore regions. *Bulletin of the Seismological Society of*  
 1047 *America*, 103(4), 2520–2533.
- 1048 Rodgers, D., & Little, T. (2006). World’s largest coseismic strike-slip offset: The  
 1049 1855 rupture of the Wairarapa Fault, New Zealand, and implications for dis-  
 1050 placement/length scaling of continental earthquakes. *Journal of Geophysical*  
 1051 *Research: Solid Earth*, 111(B12).
- 1052 Romanet, P., & Ide, S. (2019). Ambient tectonic tremors in Manawatu, Cape Tur-  
 1053 nagain, Marlborough, and Puysegur, New Zealand. *Earth, Planets and Space*,  
 1054 71(1), 1–9.
- 1055 Senobari, N. S., Funning, G. J., Keogh, E., Zhu, Y., Yeh, C.-C. M., Zimmerman,  
 1056 Z., & Mueen, A. (2019). Super-Efficient Cross-Correlation (SEC-C): A fast  
 1057 matched filtering code suitable for desktop computers. *Seismological Research*  
 1058 *Letters*, 90(1), 322–334.
- 1059 Stirling, M., McVerry, G., Gerstenberger, M., Litchfield, N., Van Dissen, R., Berry-  
 1060 man, K., ... others (2012). National seismic hazard model for New Zealand:  
 1061 2010 update. *Bulletin of the Seismological Society of America*, 102(4), 1514–  
 1062 1542.
- 1063 Tan, F., Ge, Z., Kao, H., & Nissen, E. (2019). Validation of the 3-D phase-weighted  
 1064 relative back projection technique and its application to the 2016 M w 7.8  
 1065 Kaikōura Earthquake. *Geophysical Journal International*, 217(1), 375–388.
- 1066 Townend, J., Sherburn, S., Arnold, R., Boese, C., & Woods, L. (2012). Three-  
 1067 dimensional variations in present-day tectonic stress along the Australia–  
 1068 Pacific plate boundary in New Zealand. *Earth and Planetary Science Letters*,  
 1069 353, 47–59.
- 1070 Trugman, D. T., & Shearer, P. M. (2017). GrowClust: A hierarchical clustering  
 1071 algorithm for relative earthquake relocation, with application to the Spanish  
 1072 Springs and Sheldon, Nevada, earthquake sequences. *Seismological Research*  
 1073 *Letters*, 88(2A), 379–391.
- 1074 Ulrich, T., Gabriel, A.-A., Ampuero, J.-P., & Xu, W. (2019). Dynamic viability of  
 1075 the 2016 Mw 7.8 Kaikōura earthquake cascade on weak crustal faults. *Nature*  
 1076 *Communications*. doi: 10.1038/s41467-019-09125
- 1077 Van Dissen, R., & Nicol, A. (2009). Mid-late Holocene paleoseismicity of the east-  
 1078 ern Clarence Fault, Marlborough, New Zealand. *New Zealand Journal of Geol-*  
 1079 *ogy and Geophysics*, 52(3), 195–208.
- 1080 Van Dissen, R., & Yeats, R. S. (1991). Hope fault, Jordan thrust, and uplift of the  
 1081 seaward Kaikoura Range, New Zealand. *Geology*, 19(4), 393–396.
- 1082 Waldhauser, F., & Ellsworth, W. L. (2000). A double-difference earthquake location

- 1083 algorithm: Method and application to the northern Hayward fault, California.  
 1084 *Bulletin of the Seismological Society of America*, 90(6), 1353–1368.
- 1085 Wallace, L. M., Hreinsdóttir, S., Ellis, S., Hamling, I., D’Anastasio, E., & Denys, P.  
 1086 (2018). Triggered Slow Slip and Afterslip on the Southern Hikurangi Subduction  
 1087 Zone Following the Kaikōura Earthquake. *Geophysical Research Letters*,  
 1088 45(10), 4710–4718. Retrieved from [https://agupubs.onlinelibrary.wiley](https://agupubs.onlinelibrary.wiley.com/doi/abs/10.1002/2018GL077385)  
 1089 [.com/doi/abs/10.1002/2018GL077385](https://agupubs.onlinelibrary.wiley.com/doi/abs/10.1002/2018GL077385) doi: 10.1002/2018GL077385
- 1090 Wallace, L. M., Kaneko, Y., Hreinsdóttir, S., Hamling, I., Peng, Z., Bartlow, N., ...  
 1091 Fry, B. (2017). Large-scale dynamic triggering of shallow slow slip enhanced by  
 1092 overlying sedimentary wedge. *Nature Geoscience*. doi: 10.1038/NNGEO3021
- 1093 Walsh, D., Arnold, R., & Townend, J. (2009). A Bayesian approach to determining  
 1094 and parametrizing earthquake focal mechanisms. *Geophysical Journal International*,  
 1095 176(1), 235–255.
- 1096 Wang, D., Chen, Y., Wang, Q., & Mori, J. (2018). Complex rupture of the 13  
 1097 November 2016 Mw 7.8 Kaikoura, New Zealand earthquake: Comparison of  
 1098 high-frequency and low-frequency observations. *Tectonophysics*, 733, 100–107.  
 1099 Retrieved from [https://www.sciencedirect.com/science/article/pii/](https://www.sciencedirect.com/science/article/pii/S0040195118300647)  
 1100 [S0040195118300647](https://www.sciencedirect.com/science/article/pii/S0040195118300647) (Physics of Earthquake Rupture Propagation) doi:  
 1101 <https://doi.org/10.1016/j.tecto.2018.02.004>
- 1102 Wang, T., Jiao, L., Tapponnier, P., Shi, X., & Wei, S. (2020). Space Imaging  
 1103 Geodesy Reveals Near Circular, Coseismic Block Rotation During the 2016  
 1104 Mw 7.8 Kaikōura Earthquake, New Zealand. *Geophysical Research Letters*,  
 1105 47(22), e2020GL090206.
- 1106 Wang, T., Wei, S., Shi, X., Qiu, Q., Li, L., Peng, D., ... Barbot, S. (2018). The  
 1107 2016 Kaikōura earthquake: Simultaneous rupture of the subduction interface  
 1108 and overlying faults. *Earth and Planetary Science Letters*, 482, 44–51.
- 1109 Warren-Smith, E., Chamberlain, C. J., Lamb, S., & Townend, J. (2017). High-  
 1110 precision analysis of an aftershock sequence using matched-filter detection:  
 1111 The 4 May 2015 ML 6 Wanaka earthquake, Southern Alps, New Zealand.  
 1112 *Seismological Research Letters*, 88(4), 1065–1077.
- 1113 Wesnousky, S. G. (2006). Predicting the endpoints of earthquake ruptures. *Nature*,  
 1114 444(7117), 358–360.
- 1115 Wiemer, Stefan and Wyss, Max. (2000). Minimum magnitude of completeness in  
 1116 earthquake catalogs: Examples from Alaska, the western United States, and  
 1117 Japan. *Bulletin of the Seismological Society of America*, 90(4), 859–869.
- 1118 Williams, C. A., Eberhart-Phillips, D., Bannister, S., Barker, D. H. N., Henrys, S.,  
 1119 Reyners, M., & Sutherland, R. (2013). Revised interface geometry for the  
 1120 Hikurangi subduction zone, New Zealand. *Seismological Research Letters*,  
 1121 84(6), 1066–1073.
- 1122 Williams, J. N., Barrell, D. J. A., Stirling, M. W., Sauer, K. M., Duke, G. C., &  
 1123 Hao, K. X. (2018, 06). Surface Rupture of the Hundalee Fault during the  
 1124 2016 Mw 7.8 Kaikōura Earthquake. *Bulletin of the Seismological Society of*  
 1125 *America*, 108(3B), 1540–1555. Retrieved from [https://doi.org/10.1785/](https://doi.org/10.1785/0120170291)  
 1126 [0120170291](https://doi.org/10.1785/0120170291) doi: 10.1785/0120170291
- 1127 Xu, W., Feng, G., Meng, L., Zhang, A., Ampuero, J. P., Bürgmann, R., & Fang, L.  
 1128 (2018). Transpressional Rupture Cascade of the 2016 Mw 7.8 Kaikoura Earth-  
 1129 quake, New Zealand. *Journal of Geophysical Research: Solid Earth*, 123(3),  
 1130 2396–2409. Retrieved from [https://agupubs.onlinelibrary.wiley.com/](https://agupubs.onlinelibrary.wiley.com/doi/abs/10.1002/2017JB015168)  
 1131 [doi/abs/10.1002/2017JB015168](https://agupubs.onlinelibrary.wiley.com/doi/abs/10.1002/2017JB015168) doi: 10.1002/2017JB015168
- 1132 Yao, D., Peng, Z., Kaneko, Y., Fry, B., & Meng, X. (2021). Dynamic triggering of  
 1133 earthquakes in the North Island of New Zealand following the 2016 Mw 7.8  
 1134 Kaikōura earthquake. *Earth and Planetary Science Letters*, 557, 116723.
- 1135 Yu, C., Li, Z., & Penna, N. T. (2020). Triggered afterslip on the southern Hikurangi  
 1136 subduction interface following the 2016 Kaikōura earthquake from InSAR time  
 1137 series with atmospheric corrections. *Remote Sensing of Environment*, 251,

1138 112097.  
1139 Zinke, R., Hollingsworth, J., Dolan, J. F., & Van Dissen, R. (2019). Three-  
1140 dimensional surface deformation in the 2016 MW 7.8 Kaikōura, New Zealand,  
1141 earthquake from optical image correlation: Implications for strain localization  
1142 and long-term evolution of the Pacific-Australian plate boundary. *Geochem-*  
1143 *istry, Geophysics, Geosystems*, 20(3), 1609–1628.